

THE *FERMI* BUBBLES. I. POSSIBLE EVIDENCE FOR RECENT AGN JET ACTIVITY IN THE GALAXY

FULAI GUO¹ AND WILLIAM G. MATHEWS¹

Draft version February 7, 2022

ABSTRACT

The *Fermi Gamma-ray Space Telescope* reveals two large gamma-ray bubbles in the Galaxy, which extend about 50° (~ 10 kpc) above and below the Galactic center and are symmetric about the Galactic plane. Using axisymmetric hydrodynamic simulations with a self-consistent treatment of the dynamical cosmic ray (CR) - gas interaction, we show that the bubbles can be created with a recent AGN jet activity about 1 - 3 Myr ago, which was active for a duration of ~ 0.1 - 0.5 Myr. The bipolar jets were ejected into the Galactic halo along the rotation axis of the Galaxy. Near the Galactic center, the jets must be moderately light with a typical density contrast $0.001 \lesssim \eta \lesssim 0.1$ relative to the ambient hot gas. The jets are energetically dominated by kinetic energy, and over-pressured with either CR or thermal pressure which induces lateral jet expansion, creating fat CR bubbles as observed. The sharp edges of the bubbles imply that CR diffusion across the bubble surface is strongly suppressed. The jet activity induces a strong shock, which heats and compresses the ambient gas in the Galactic halo, potentially explaining the *ROSAT* X-ray shell features surrounding the bubbles. The *Fermi* bubbles provide plausible evidence for a recent powerful AGN jet activity in our Galaxy, shedding new insights into the origin of the halo CR population and the channel through which massive black holes in disk galaxies release feedback energy during their growth.

Subject headings: cosmic rays – galaxies: active – galaxies: jets – Galaxy: nucleus – gamma rays: galaxies

1. INTRODUCTION

Using 1.6 years of data from the *Fermi Gamma-ray Space Telescope*, Su et al. (2010) discovered two large gamma-ray bubbles emitting at $1 \lesssim E_\gamma \lesssim 100$ GeV in our Galaxy. They are denoted as the ‘*Fermi* bubbles’, and extend to $\sim 50^\circ$ above and below the Galactic center (GC), with a width of about 40° in longitude. They have approximately uniform gamma ray surface brightness with sharp edges. The bubbles were previously identified as the ‘*Fermi* haze’ from the first year *Fermi* data (Dobler et al. 2010). The gamma-ray emission associated with the bubbles has a hard spectrum ($dN_\gamma/dE_\gamma \sim E_\gamma^{-2}$) and could originate from cosmic ray (CR) protons and/or CR electrons. CR protons may collide with thermal nuclei inelastically, producing neutral pions which decay into gamma rays (Crocker & Aharonian 2011). For the latter, gamma rays can be produced by the inverse Compton (IC) scattering of CR electrons with the interstellar radiation field (ISRF) and the cosmic microwave background (CMB; Dobler et al. 2010, Su et al. 2010). The CR electron (CRe) population also produces microwave synchrotron radiation, which was previously invoked to explain the microwave haze (at tens of GHz) discovered by the *Wilkinson Microwave Anisotropy Probe* (WMAP) - the ‘WMAP haze’, which is spatially associated with the *Fermi* bubbles (Finkbeiner 2004; Dobler & Finkbeiner 2008).

The bilobular morphology of the *Fermi* bubbles suggests that the responsible CR population is not made of diffused CRs originally accelerated by supernova (SN) shocks in the Galactic plane. SN CRs diffusing into the

Galactic halo would likely have a much different spatial distribution, and tend to form one single CR-filled bubble centered at the GC. Furthermore, the sharp edges of the *Fermi* bubbles imply that the diffusion is strongly suppressed across the bubble surface, and thus is not the primary reason for the bubble expansion/formation (see Section 3.2). Similarly, the morphology and sharp edges of the *Fermi* bubbles suggest that the main CR population in the *Fermi* bubbles is not byproducts of dark matter annihilations.

As pointed out by Su et al. (2010), the *Fermi* bubbles were most likely created by some large episode of energy injection in the GC, e.g., jets originating from an active galactic nucleus (AGN) activity or a nuclear starburst. Here we perform the first dynamical study of the jet scenario. Our opposing jet model for the *Fermi* bubbles is inspired by similar non-thermal double jet events observed in massive galaxies, particularly those lying at the centers of galaxy groups and clusters (McNamara & Nulsen 2007). AGN jets have been previously proposed to explain extended extragalactic radio sources (Longair et al. 1973; Scheuer 1974; Blandford & Rees 1974). It is well known that AGN jets carry a significant amount of high energy CRs, which have been seen from radio synchrotron emission, and many AGN jets have also been observed to actively create CR-filled bubbles (e.g., the jets in Cygnus A and many Fanaroff-Riley type I radio sources as in Laing et al. 2006). However, due to its limited sensitivity and resolution, gamma-ray observation can not easily detect AGN bubbles. The proximity of the *Fermi* bubbles may provide a special opportunity to thoroughly study AGN bubbles in gamma ray bands.

In this paper we use hydrodynamic simulations to perform a feasibility study, investigating if the main mor-

¹ UCO/Lick Observatory, Department of Astronomy and Astrophysics, University of California, Santa Cruz, CA 95064, USA; fulai@ucolick.org

phological features of the *Fermi* bubbles can be reproduced by a recent AGN jet activity from the GC. Our calculations take into account the dynamical interactions between CRs and thermal gas, self-consistently modeling the CR advection with the thermal gas. Our two-dimensional (2D) calculations allow us to do a fast parameter study, identifying appropriate jet parameters. We show that to reproduce the morphology of *Fermi* bubbles, successful AGN jets cannot be either too massive or too light, but are constrained to have densities about 0.001 - 0.1 times the density of the initial ambient hot gas near the GC (i.e., with density contrasts $0.001 \lesssim \eta \lesssim 0.1$). In particular, the observed *Fermi* bubbles can be approximately reproduced by a pair of bipolar AGN jets which began about 1 - 3 Myr ago, and were active for a duration of ~ 0.1 - 0.5 Myr. The total AGN energy released in our fiducial run A1 is $\sim 10^{57}$ erg, but it scales with the uncertain density of the original gas in the Galactic halo, probably varying between about 10^{55} and 10^{57} erg. We also show that to produce the sharp outer edges of the bubbles seen in gamma ray emission, CR diffusion across the bubble boundaries must be strongly suppressed below the CR diffusivity observed in the solar vicinity.

Similar to other astronomical phenomena, the *Fermi* bubbles may result from the interplay of various physical mechanisms. Including hydrodynamics, CR dynamics, CR advection and diffusion, this paper mainly explores the potentially dominant physics involved in the formation of the *Fermi* bubbles – a pair of opposing jets. We follow the dynamical evolution of the jets, and investigate the success and problems of the basic jet model by directly comparing with detailed observational features of the *Fermi* bubbles. We also investigate the degeneracies and uncertainties associated with the jet model. In a companion paper (Guo et al. 2012; hereafter denoted as “Paper II”), we investigate the roles of additional physics – shear viscosity and CR diffusion on the evolution of the *Fermi* bubbles, exploring potential solutions for the observational discrepancies associated with this basic jet scenario. The rest of the paper is organized as follows. In Section 2, we describe CR transport in the Galaxy, our Galactic model, and numerical setup. We present our results in Section 3, and summarize our main conclusions with implications in Section 4.

2. THE MODEL AND NUMERICAL METHODS

2.1. Cosmic Ray Transport in the Galaxy

The observed *Fermi* bubbles are offset from the GC with one above and the other below the Galactic plane. They extend to about 50° (~ 10 kpc) above and below the GC, and are symmetric about the Galactic plane. Here we assume that the distance from the Sun to the GC is $R_\odot = 8.5$ kpc. In *Fermi* maps, the bubbles are seen at $1 \lesssim E_\gamma \lesssim 100$ GeV, corresponding to relativistic CRs with energies $10 \lesssim E_{\text{cr}} \lesssim 100$ GeV if the observed γ rays are inverse Compton upscattering of starlight by these CRs. The IC cooling time of these CR electrons is typically a few million years, depending on their energies and locations (see Figure 28 of Su et al. 2010). Due to the short age and symmetry of these two bubbles, they probably share the same origin. The CRs may be accelerated or reaccelerated in situ in these two bubbles

(Mertsch & Sarkar 2011), but one potential problem for this scenario is to explain how turbulence is triggered roughly simultaneously in *two bubble-shaped regions* separated by such a large distance (~ 10 kpc). Here we consider a different scenario where CRs are produced by one single event and then transported to these two bubbles. If this scenario is correct, it is likely that the CRs were originated from the midpoint between the bubbles, the GC.

Each CR particle has a velocity near the speed of light. However, it is well known that the collective transport speed of CRs in the Galaxy is much smaller (e.g., CRs reaching the Earth are observed to be highly isotropic). This is commonly explained by the scattering of CRs by magnetic irregularities. When the scattering is significant, CRs are strongly trapped and ‘effectively’ move with magnetic irregularities, which are frozen in the hot plasma. Therefore, CRs are advected with thermal gas at the local gas velocity, and in this case, the CR transport is usually called advection. In regions where the magnetic field is locally aligned, CRs may stream through thermal gas, but the streaming speed is limited by the Alfvén speed. If CRs stream along the magnetic field lines at a speed faster than the local Alfvén speed, the CR streaming instability is triggered and excites Alfvén waves, which significantly scatter CRs in return (Skilling 1971; also see Kuhrud 2005, Chap. 12). Consequently, the CR streaming speed relative to the gas is roughly the local Alfvén speed. Due to the unknown and possibly complex magnetic field structure, CR streaming relative to the local gas is often ignored, as we assume in this paper. This is a good approximation in many cases, where CR scattering off magnetic irregularities is significant and/or the Alfvén speed is much smaller than the local gas speed.

In addition to advection, CRs can also diffuse through the thermal gas, as they scatter off magnetic inhomogeneities. CR diffusion is usually described by the CR diffusion coefficient κ , which probably depends on the magnetic field structure and CR energy. Typical values of κ for 1 GeV CRs are found to be $\kappa \sim (3 - 5) \times 10^{28} \text{ cm}^2 \text{ s}^{-1}$ in the solar vicinity (Strong et al. 2007).

The *Fermi* bubbles extend up to ~ 10 kpc away from the GC. If the CRs in the bubbles are produced at the GC, they must be transported very quickly, at a speed of $v_{\text{transport}} \sim 10 \text{ kpc}/t_{\text{age}} \sim 10000(t_{\text{age}}/1 \text{ Myr})^{-1} \text{ km/s}$, to form the bubbles, where t_{age} is the age of the *Fermi* bubbles. We expect t_{age} to be less than a few million years due to the short IC cooling times of CRs responsible for the detected γ -ray emission. Obviously, the main CR transport mechanism is not diffusion, which would form one single gamma-ray bubble centered at the GC and is too slow to transport CRs. To transport CRs for a distance of $l = 10$ kpc within t_{age} by diffusion, the required diffusion coefficient is $\kappa \sim l^2/t_{\text{age}} \sim 3 \times 10^{31}(t_{\text{age}}/1 \text{ Myr})^{-1} \text{ cm}^2 \text{ s}^{-1}$, three orders of magnitude larger than typical estimates of the CR diffusivity in the Galaxy. Furthermore, diffusion tends to produce blurred boundaries across which the CR density varies gradually, while the observed *Fermi* bubbles have very sharp edges in gamma rays.

Since diffusion is not responsible for transporting CRs from the GC to the *Fermi* bubbles, advection of CRs

with thermal gas is the only possible CR transport mechanism. Strong CR advection may be induced by galactic winds or AGN jets from the GC. Galactic winds are often detected through absorption lines of their cold gaseous components, which typically have speeds of about $200\text{--}300\text{ km s}^{-1}$ (Martin 2005), more than one order of magnitude below the required CR transport speed for the *Fermi* bubbles: $v_{\text{transport}} \sim 10000(t_{\text{age}}/1\text{ Myr})^{-1}\text{ km/s}$. However, starburst winds usually contain multi-temperature components and some hot components may have much larger speeds (Strickland & Heckman 2009). Some winds have indeed been observed to have velocities slightly beyond 1000 km/s , particularly those probably driven by radiation or mechanical energy of AGN events (e.g., Rupke & Veilleux 2011). A thermally driven starburst wind flowing at the speed of $v_{\text{transport}}$ would require gas with comparable sound speeds and temperatures $T \sim 4 \times 10^9\text{ K}$ that are unreasonably high. Alternatively, the wind scenario may be viable if the gamma-ray emission from the *Fermi* bubbles is mainly contributed by the decay of neutral pions produced during the hadronic collisions of CR protons with thermal nuclei (Crocker & Aharonian 2011). One potential challenge for the wind scenario is that winds often contain low-temperature gas as seen in $\text{H}\alpha$, molecular, and X-ray filamentary structures, which have not yet been observed in the *Fermi* bubbles.

In this paper we consider an alternative scenario where CRs are transported by AGN jets, which typically have relativistic or sub-relativistic velocities on parsec and kpc scales, much faster than galactic winds. The propagation of AGN jets is determined by the speed of hotspots at the jet extremities, and may be close to $v_{\text{transport}}$, depending on both jet parameters and the ambient gas properties. The primary goal of our paper is to study with numerical simulations the possibility of forming the *Fermi* bubbles with CR-carrying AGN jets from the GC. CRs in AGN jets may be dominated by the electron-proton plasma or electron-positron plasma. It is unclear if CR protons or electrons dominate the gamma-ray emission from the *Fermi* bubbles. In this paper we focus on the morphology and dynamical evolution of the *Fermi* bubbles, leaving studies of the particle content and gamma-ray emission mechanisms to the future.

CR transport in the Galaxy has been studied numerically by some simulation codes, in particular, the Galactic Propagation (GALPROP) code (Strong & Moskalenko 1998), which is very detailed, including three-dimensional distributions of gas, dust, magnetic fields, optical and FIR photons. However, GALPROP is not able to self-consistently model CR advection, which is important when significant gas motions are present. In addition to jet motions, CR pressure gradients can also produce gas motions, which in turn advect the CRs. Thus, dynamical interactions between CRs and the background gas should be taken into account to self-consistently model CR transport, particularly advection.

We have developed a finite-differencing code to numerically study CR transport and the dynamical interaction between CRs and hot gas, which has been successfully used to study X-ray cavities and radio bubbles in galaxy clusters in a series of papers, e.g., Mathews & Brighenti (2008a), Mathews & Brighenti (2008b), Mathews (2009), Guo & Mathews (2010a), Guo & Mathews (2010b), and

Mathews & Guo (2010). More recently, we use our code to study the evolution of CR-dominated AGN jets in galaxy clusters in Guo & Mathews (2011). In this paper, we intend to modify our code to study AGN jets and the formation of *Fermi* bubbles in the Milky Way. In the rest of this section, we will elaborate the basic equations and assumptions of our model, and the setup of our numerical procedure.

2.2. Equations and Assumptions

The dynamical interaction between CRs and thermal gas may be described by the CR pressure P_c . In our calculations, we directly follow the temporal and spatial evolution of the CR energy density e_c , which is related to P_c through $P_c = (\gamma_c - 1)e_c$, where $\gamma_c = 4/3$. The nature of the relativistic particles with energy density e_c is unspecified and may be electrons and/or protons with any spectra. Of course the equation of state may be somewhat harder if e_c is mainly contributed by trans-relativistic protons at $\sim 1\text{ GeV}$. CR pressure gradients can accelerate thermal gas, converting CR energy into the kinetic energy of thermal gas, which may be further converted to the internal gas energy in shocks or other compressions. The combined hydrodynamic evolution of thermal gas and CRs can be described by the following four equations:

$$\frac{d\rho}{dt} + \rho \nabla \cdot \mathbf{v} = 0, \quad (1)$$

$$\rho \frac{d\mathbf{v}}{dt} = -\nabla(P + P_c) - \rho \nabla \Phi, \quad (2)$$

$$\frac{\partial e}{\partial t} + \nabla \cdot (e\mathbf{v}) = -P \nabla \cdot \mathbf{v}, \quad (3)$$

$$\frac{\partial e_c}{\partial t} + \nabla \cdot (e_c \mathbf{v}) = -P_c \nabla \cdot \mathbf{v} + \nabla \cdot (\kappa \nabla e_c), \quad (4)$$

where $d/dt \equiv \partial/\partial t + \mathbf{v} \cdot \nabla$ is the Lagrangian time derivative, κ is the CR diffusion coefficient, and all other variables have their usual meanings. The gas pressure P is related to the gas internal energy density e via $P = (\gamma - 1)e$, where we assume $\gamma = 5/3$.

The Galactic potential Φ is mainly contributed by three components: the bulge, disk and dark matter halo. We assume that it is fixed with time and neglect the small contribution from hot halo gas. Our simple Galactic potential model and initial conditions for the thermal gas are explained in Section 2.3. We ignore radiative cooling of thermal gas, which is unimportant during the short-duration ($\lesssim 1\text{--}3\text{ Myr}$) of our simulations. The gas temperature is related to the gas pressure and density via the ideal gas law:

$$T = \frac{\mu m_\mu P}{k_B \rho}, \quad (5)$$

where k_B is Boltzmann's constant, m_μ is the atomic mass unit, and $\mu = 0.61$ is the molecular weight. To avoid confusion we denote the gas pressure P as P_g in the rest of the paper.

At time $t = 0$ we assume that the CR energy density is zero in the Galaxy, $e_c = 0$, but at later times CRs enter the Galactic halo in jets from the GC. Equation 4 describes the evolution of CR energy density including both advection and diffusion. CR diffusion depends on the magnetic field structure and may be anisotropic, but for simplicity, we generally assume that it is isotropic and the CR diffusion coefficient κ is a constant in space and time: $\kappa \sim 3 \times 10^{27} - 3 \times 10^{29} \text{ cm}^2 \text{ s}^{-1}$ (see Table 1). We explore how the value of κ affects the formation and morphology of *Fermi* bubbles in Section 3.2, where we also consider a case with a spatially-varying diffusion coefficient. κ may also depend on CR energy, which may affect the gamma-ray spectrum and the evolution of the *Fermi* bubbles. This effect is not studied in this paper.

As discussed in the previous subsection, CRs interact with magnetic irregularities and Alfvén waves, effectively exerting CR pressure gradients on the thermal gas (equation 2). Pressure gradients in the CR component act directly on the gas by means of magnetic fields frozen into the gas. This is the primary interaction between CRs and thermal gas. We neglect other more complicated (probably secondary) interactions, e.g., Coulomb interactions, hadronic collisions, and hydromagnetic-wave-mediated CR heating, that all depend on the CR energy spectrum (e.g., Guo & Oh 2008). Since the jet evolution in our calculation is mainly driven by its kinetic energy and the injected CR energy, the dynamical effect of magnetic fields is expected to be moderate and is unlikely to significantly alter our results (see our estimates in Section 3.1). More sophisticated magnetohydrodynamical calculations are necessary in the future to explore the impact of magnetic fields. We also neglect CR energy losses from synchrotron and IC emissions. Although the cooling is important for TeV electrons, its impact on the integrated CR energy density e_c is expected to be small, i.e., the main contribution to e_c may be low-energy CR electrons (e.g., at $\sim 0.1 - 100 \text{ GeV}$) and possibly CR protons, which have much longer lifetimes. If TeV electrons contribute significantly to the gamma-ray emission of the *Fermi* bubbles, CR cooling may have an important effect on the temporal evolution of the gamma ray emission (both intensity and spectrum), which is beyond the scope of the current paper.

2.3. The Galactic Model

Our key objective in this paper is to perform a feasibility study to determine if the *Fermi* bubbles can be created with jets from the GC that are apparently no longer active. The *Fermi* bubbles are inertially confined by pre-existing gas in the Galactic halo having (virial) temperatures of $\sim 10^6 \text{ K}$. For simplicity, we assume that the hot gaseous halo is initially isothermal with temperature $T = 2.4 \times 10^6 \text{ K}$, as inferred from X-ray absorption line studies (Yao & Wang 2005). To derive the initial density distribution of the hot gas, we further assume that the gas is initially in hydrostatic equilibrium. We adopt the Galactic potential from Helmi & White (2001), where the Galaxy is represented by a fixed potential with three components: a dark logarithmic halo

$$\Phi_{\text{halo}} = v_{\text{halo}}^2 \ln(r^2 + d_h^2), \quad (6)$$

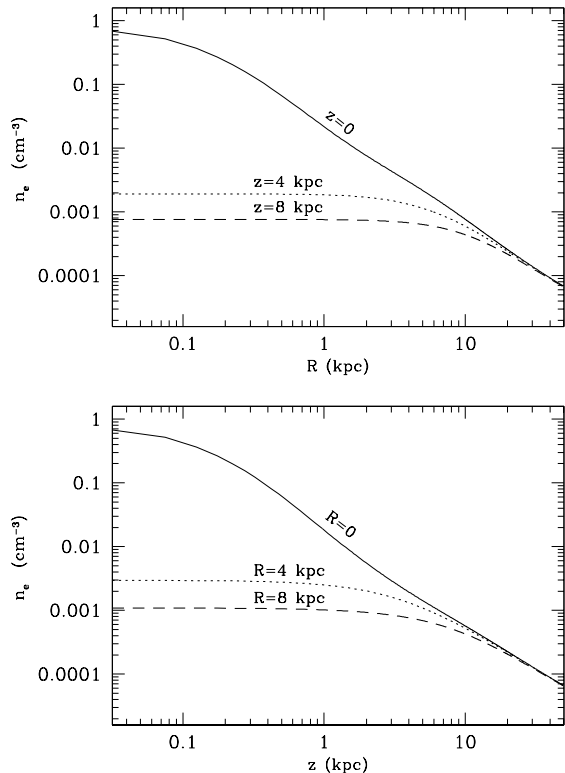


FIG. 1.— Initial profiles of electron number density of the hot gas in the Galactic halo along the R direction (parallel to the Galactic plane) at three fixed values of z (top panel) and along the z direction (perpendicular to the Galactic plane) at three fixed values of R (bottom panel) in all simulations except run A5, where the gas density is lower by a factor of 100. The density distribution $n_e(R, z)$ is solved from hydrostatic equilibrium, a spatially uniform temperature $T = 2.4 \times 10^6 \text{ K}$, and a given value for the electron number density at the origin, n_{e0} (chosen to be 1 cm^{-3} in all runs except run A5).

a Miyamoto-Nagai disk

$$\Phi_{\text{disc}} = -\frac{GM_{\text{disc}}}{\sqrt{R^2 + (a + \sqrt{z^2 + b^2})^2}}, \quad (7)$$

and a spherical Hernquist stellar bulge

$$\Phi_{\text{bulge}} = -\frac{GM_{\text{bulge}}}{r + d_b}, \quad (8)$$

where R is the galactocentric radius in the Galactic plane, $r = \sqrt{R^2 + z^2}$ is the spatial distance to the GC, $v_{\text{halo}} = 131.5 \text{ km s}^{-1}$ and $d_h = 12 \text{ kpc}$; $M_{\text{disc}} = 10^{11} M_{\odot}$, $a = 6.5 \text{ kpc}$ and $b = 0.26 \text{ kpc}$; $M_{\text{bulge}} = 3.4 \times 10^{10} M_{\odot}$ and $d_b = 0.7 \text{ kpc}$. We have also explored alternative models of the Galactic potential from Breitschwerdt et al. (1991) and Wolfire et al. (1995), and found that the resulting gas density distribution is similar.

For the hot gas, it is convenient to use the electron number density n_e , which is related to the gas density through

$$\rho = \mu_e n_e m_{\mu}, \quad (9)$$

where $\mu_e = 5\mu/(2 + \mu)$ is the molecular weight per electron. For a given value of electron number density at the origin n_{e0} , we derive the spatial distribution of n_e from hydrostatic equilibrium and the spatially-uniform temperature $T = 2.4 \times 10^6 \text{ K}$. In all simulations except

run A5, we adopt the n_e distribution with $n_{e0} = 1 \text{ cm}^{-3}$, which gives electron number densities on the order of 10^{-3} cm^{-3} at galactocentric distances of a few kpc. Figure 1 shows the resulting n_e profiles along the R direction for three fixed values of z and along the z direction for three fixed values of R . We have also explored simulations with different values of n_{e0} , and found that, to reproduce the morphology of the observed *Fermi* bubbles, the required jet power scales with n_{e0} (i.e., with the densities of the hot halo gas; see discussions in Sec. 3.3). In run A5, we choose $n_{e0} = 0.01 \text{ cm}^{-3}$, explicitly exploring the dependence of our results on the density of halo gas. The unknown density distribution of hot halo gas is a major uncertainty in constraining the energetics of the *Fermi* bubble event. The observed gamma-ray surface brightness can in principle put a lower limit on the CR energy density within the bubbles, which may be used to constrain the properties of the hot halo gas and the local density of ISRF photons that are IC upscattered.

2.4. Numerical Setup and Jet Injection

Equations (1) – (4) are solved in (R, z) cylindrical coordinates using a 2D axisymmetric Eulerian code similar to ZEUS 2D (Stone & Norman 1992). In particular, our code follows the evolution of both hot gas and CRs, implementing their dynamical interaction, CR diffusion, and an energy equation for CRs. The CR diffusion is solved by using operator-splitting and a fully implicit Crank-Nicolson differencing method. While this differencing scheme is stable, we restrict each time step by the stability condition for explicitly differenced diffusion, as well as Courant conditions for numerical stability. The computational grid consists of 400 equally spaced zones in both coordinates out to 20 kpc plus additional 100 logarithmically-spaced zones out to 50 kpc. The central 20 kpc in each direction is resolved to 0.05 kpc. For both thermal and CR fluids, we adopt outflow boundary conditions at the outer boundary and reflective boundary conditions at the inner boundary.

The jet inflow is introduced with a constant speed v_{jet} along the z -axis (the rotation axis of the Galaxy) from the GC. During the active AGN phase $0 \leq t \leq t_{\text{jet}}$, the jet is initialized in a cylinder on the computational grid with radius R_{jet} and length z_{jet} beginning at the GC. All the physical variables in this cylinder are updated uniformly with the jet parameters at every time step during this phase. The jet contains both thermal gas and relativistic CRs, which are initialized inside the jet source cylinder and injected into the Galaxy at $z = z_{\text{jet}}$ with the jet speed v_{jet} having an initial opening angle of 0° . In the simulations presented in this paper, we take $z_{\text{jet}} = 0.5 \text{ kpc}$. This allows us to avoid modeling the complex jet evolution closer to the GC, which would require higher spatial resolution and involves uncertain multi-phase gas properties. We further assume that the jet has undergone significant deceleration and transverse expansion within the jet source region ($0 \lesssim z \lesssim z_{\text{jet}}$), as seen in some extragalactic AGN jets (e.g., Laing et al. 2006). In our calculations, we thus investigate jets with $R_{\text{jet}}/z_{\text{jet}} \sim 0.2 - 1$ and $v_{\text{jet}}/c \sim 0.05 - 0.3$, where c is the speed of light. However, it is still possible that AGN jets from the GC may have much higher velocities at z_{jet} . Such jets are beyond the scope of this paper – our primary purpose is to perform a simple feasibility study

to investigate if the location, size and morphology of the observed *Fermi* bubbles can be reproduced by a jet event within a few Myrs.

We stop the calculation at the current age of the *Fermi* bubbles $t = t_{\text{Fermi}}$, which is defined as the time when the produced CR bubble reaches the most distant boundary of the observed northern *Fermi* bubble along the jet axis. The bubble age t_{Fermi} is constrained to be less than a few million years by the short IC cooling times of the gamma-ray-emitting CRs within the bubbles. In this paper we only consider models with $t_{\text{Fermi}} \lesssim 3 \text{ Myr}$ (the estimated IC cooling time of $\sim 100 \text{ GeV}$ electrons at $z \sim 4 \text{ kpc}$; see Fig. 28 of Su et al. 2010), though it may be dynamically possible to create the *Fermi* bubbles with a current age more than 3 Myr. Alternatively, if the gamma-ray emission from the *Fermi* bubbles is mainly contributed by CR-proton-induced pion decay, the age of the *Fermi* bubbles could be much longer (see Crocker & Aharonian 2011).

The initial jet is described by six parameters: the thermal gas density ρ_j , the gas energy density e_j , the CR energy density e_{cr} , the jet velocity v_{jet} , the jet radius R_{jet} , and the jet duration t_{jet} . From ρ_j , one can derive the commonly-used jet density contrast between thermal gas inside the jet and the ambient hot gas: $\eta = \rho_j/\rho_{\text{amb}}$, where ρ_{amb} is the initial halo gas density at $(R, z) = (0, z_{\text{jet}})$. The jet power can be written as

$$P_{\text{jet}} = P_{\text{ke}} + P_{\text{cr}} + P_{\text{th}}, \quad (10)$$

where $P_{\text{ke}} = \rho_j v_{\text{jet}}^3 \pi R_{\text{jet}}^2 / 2$ is the jet kinetic power, $P_{\text{cr}} = e_{\text{cr}} v_{\text{jet}} \pi R_{\text{jet}}^2$ is the jet CR power, and $P_{\text{th}} = e_j v_{\text{jet}} \pi R_{\text{jet}}^2$ is the jet thermal power. The total energy injected by the jet can be written as $E_{\text{jet}} = P_{\text{jet}} t_{\text{jet}}$. Thermal and CR energy density are related to the gas and CR pressure respectively, thus both affecting the dynamical evolution of hot gas. Therefore e_j and e_{cr} are degenerate in our simulations: we can increase one while decreasing the other, reaching similar results (see run A6; however, synchrotron and/or IC emissions from CRs can in principle break this degeneracy). In all simulation runs except run A6 (see Table 1), we take $\eta_e = e_j/e_{\text{amb}} = 1$, where e_{amb} is the initial ambient gas energy density at $(R, z) = (0, z_{\text{jet}})$. In simulations that successfully produce *Fermi* bubbles as observed, the jets are usually over-pressured relative to the ambient hot gas at $z = z_{\text{jet}}$. As explained above, the jet simulations have a very large parameter space, and our 2D calculations permit us to run a large number (more than 100) simulations with different parameters within a reasonable amount of time. Here we present a few representative calculations particularly relevant to the *Fermi* bubbles, and list their model parameters in Table 1. Some basic information of the AGN event and the resulting *Fermi* bubbles in each simulation is given in Table 2.

3. RESULTS

3.1. Forming Fermi Bubbles with AGN Jets

In this subsection, we present in detail one representative run (run A1), which approximately reproduces the morphology of the *Fermi* bubbles as observed in gamma-rays with the *Fermi* telescope. The main objective is to show that it is feasible to produce the observed *Fermi* bubbles from one single AGN jet activity from the GC.

TABLE 1
MODEL PARAMETERS IN ALL SIMULATIONS PRESENTED IN THIS PAPER

Run	n_{e0}^a (cm^{-3})	κ ($\text{cm}^2 \text{ s}^{-1}$)	R_{jet} (kpc)	t_{jet} (Myr)	η^b	η_e^c	e_{jet}^d	v_{jet}	n_{ej}^e (10^{-4} cm^{-3})
A1	1	3×10^{27}	0.4	0.3	0.01	1	1.0	0.1c	5.68
A-diff1	1	3×10^{28}	0.4	0.3	0.01	1	1.0	0.1c	5.68
A-diff2	1	3×10^{29}	0.4	0.3	0.01	1	1.0	0.1c	5.68
A-diff3	1	varied	0.4	0.3	0.01	1	1.0	0.1c	5.68
A2	1	3×10^{27}	0.4	0.3	0.02	1	1.5	0.1c	11.36
A3	1	3×10^{27}	0.4	0.2	0.01	1	3.0	0.2c	5.68
A4	1	3×10^{27}	0.2	0.3	0.05	1	6.0	0.1c	28.40
A5	0.01	3×10^{27}	0.4	0.3	0.01	1	0.01	0.1c	0.057
A6	1	3×10^{27}	0.4	0.3	0.01	9.325	0.1	0.1c	5.68
B1	1	3×10^{27}	0.4	0.3	0.0001	1	1.0	0.1c	0.057
B2	1	3×10^{27}	0.4	0.3	0.5	1	1.0	0.05c	284

^aThe initial thermal electron number density at the origin (R, z) = (0, 0), which determines the density normalization of the isothermal hydrostatic halo gas (see Sec. 2.3).

^b η determines the initial thermal gas density in the jet base $\rho_j = \eta \rho_{\text{atm}}$, where ρ_{amb} is the initial halo gas density at (R, z) = (0, z_{jet}) and z_{jet} is chosen to be 0.5 kpc in this paper (see Sec. 2.4).

^c η_e determines the initial thermal energy density in the jet base $e_j = \eta_e e_{\text{atm}}$.

^dThe initial CR energy density in the jet base (in units of $10^{-9} \text{ erg cm}^{-3}$).

^e n_{ej} is the initial thermal electron number density in the jet base: $n_{\text{ej}} = \rho_j / (\mu_e m_\mu)$, calculated from the values of η and ρ_{atm} .

TABLE 2
PROPERTIES OF THE *Fermi* BUBBLES AND THE ASSOCIATED AGN EVENT IN SIMULATION RUNS

Run	t_{Fermi} (Myr)	P_{cr}^a	P_{ke}^b	P_{jet}^c ($10^{43} \text{ erg s}^{-1}$)	E_{jet}^d (10^{56} erg)	\dot{M}_{BH}^e (M_\odot/yr)	ΔM_{BH}^f (M_\odot)	M_{jet}^g (M_\odot)
A1	2.06	1.43	7.09	8.60	8.13	0.03	9.0×10^3	1.5×10^5
A-diff1	1.94	1.43	7.09	8.60	8.13	0.03	9.0×10^3	1.5×10^5
A-diff2	1.30	1.43	7.09	8.60	8.13	0.03	9.0×10^3	1.5×10^5
A-diff3	2.06	1.43	7.09	8.60	8.13	0.03	9.0×10^3	1.5×10^5
A2	1.74	2.15	14.18	16.41	15.51	0.057	1.7×10^4	3.0×10^5
A3	0.86	8.58	56.75	65.48	41.25	0.23	6.9×10^4	2.0×10^5
A4	2.34	2.15	8.87	11.03	10.42	0.039	1.2×10^4	1.9×10^5
A5	2.06	0.014	0.071	0.086	0.081	0.0003	90	1.5×10^3
A6	2.15	0.14	7.09	7.96	7.52	0.028	8.4×10^3	1.5×10^5
B1	-	1.43	0.07	1.58	1.49	0.0055	1.7×10^3	1.5×10^3
B2	0.89	0.72	44.33	45.08	42.6	0.16	4.8×10^4	3.7×10^6

^a P_{cr} , P_{ke} , and P_{jet} are, respectively, the jet CR, kinetic, and total powers (in units of $10^{43} \text{ erg s}^{-1}$). $P_{\text{jet}} = P_{\text{ke}} + P_{\text{cr}} + P_{\text{th}}$, where the thermal jet power P_{th} is much smaller than P_{ke} and/or P_{cr} in our runs. The real jet power depends on the uncertain halo gas density, and is thus not well constrained.

^d $E_{\text{jet}} = P_{\text{jet}} t_{\text{jet}}$ is the energy injected by one jet during the AGN phase $0 \leq t \leq t_{\text{jet}}$. The total energy injected by both bipolar jets is $2E_{\text{jet}}$.

^e \dot{M}_{BH} is the corresponding accretion rate of the supermassive black hole at the GC, assuming a feedback efficiency of 10%: $\dot{M}_{\text{BH}} = 2P_{\text{jet}}/(0.1c^2)$.

^f ΔM_{BH} is the total mass accreted by the supermassive black hole at the GC during the AGN event, assuming a feedback efficiency of 10%: $\Delta M_{\text{BH}} = \dot{M}_{\text{BH}} t_{\text{jet}}$.

^g $M_{\text{jet}} = 2\rho_j \pi R_{\text{jet}}^2 v_{\text{jet}} t_{\text{jet}}$, estimated at $|z| = 0.5 \text{ kpc}$, is the total mass ejected in the two jets during the AGN event, including the potential gas entrained by the jets at $|z| < 0.5 \text{ kpc}$.

Other choices of jet parameters may produce similar results, so it is impossible to determine unique jet properties from the observed bubble morphology. Here we focus on some interesting features and problems in this representative run.

The edges of the bubbles are shown in Figure 18 of Su et al. (2010) in Galactic coordinates (l, b). To compare our simulation results with observations, we derive the edges of the bubbles in our coordinates (R, z) using the following coordinate conversion:

$$R = R_\odot |\tan(l)|, \quad (11)$$

$$z = \frac{R_\odot}{\cos(b)} \tan(b). \quad (12)$$

The resulting edge of the northern *Fermi* bubble is shown as the dotted region in each panel of Figure 2. The computed bubble is more vertically elongated in (R, z) coordinates than when viewed in Galactic coordinates since $\partial z / \partial b \sim 1/\cos^2(b)$ increases significantly with b from $b = 0$ to $b \sim 50^\circ$. The line-of-sight projection has a non-negligible effect on the coordinate conversion, since the bubble size is comparable to the distance between the Sun and the GC. The real bubble may be slightly

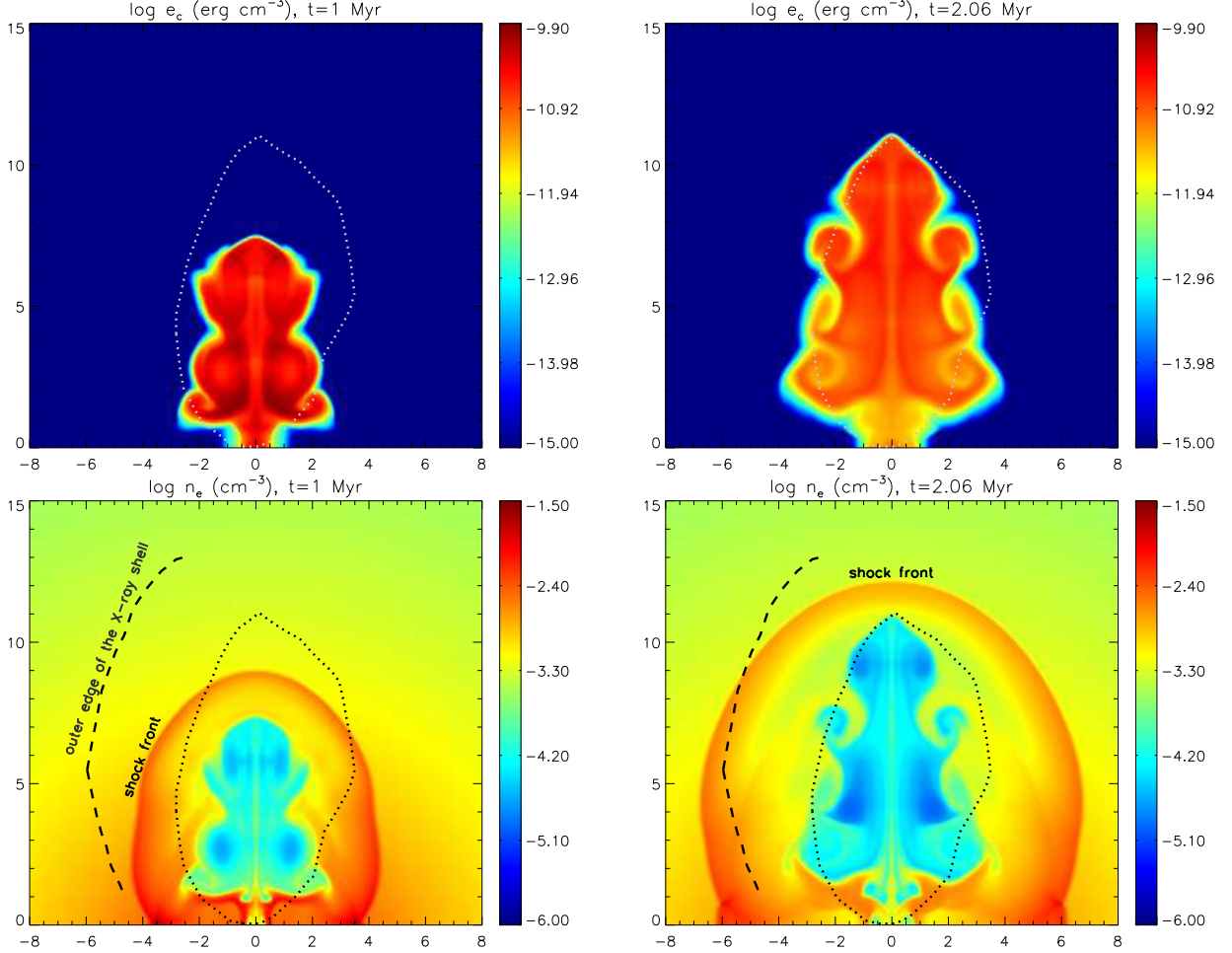


FIG. 2.— Central slices (16×15 kpc) of CR energy density (top panels) and thermal electron number density (bottom panels) in logarithmic scale in run A1 at $t = 1$ Myr (left panels), and $t = t_{\text{Fermi}} = 2.06$ Myr (right panels). Horizontal and vertical axes refer to R and z respectively, labeled in kpc. The dotted region in each panel approximately encloses the observed north *Fermi* bubble. The propagation of the AGN jet, active for only $t_{\text{jet}} = 0.3$ Myr, produces a CR bubble at $t = 2.06$ Myr approximately matching the observed *Fermi* bubble. The dashed lines in bottom panels trace the outer edge of the *ROSAT* X-ray shell feature in the northeastern direction (which is most prominent), and is roughly spatially coincident with the jet-induced shock at $t = 2.06$ Myr.

smaller than the one shown in Figure 2. An accurate account for this effect requires three-dimensional structure of the bubbles, and is much more complex. We expect this effect to be small and neglect it in this paper.

The jet parameters for the fiducial run A1 are listed below: radius $R_{\text{jet}} = 0.4$ kpc, thermal electron number density $n_{\text{ej}} = 5.68 \times 10^{-4} \text{ cm}^{-3}$, gas energy density $e_j = 5.4 \times 10^{-11} \text{ erg cm}^{-3}$, CR energy density $e_{\text{jer}} = 1.0 \times 10^{-9} \text{ erg cm}^{-3}$, velocity $v_{\text{jet}} = 0.1c$, and duration $t_{\text{jet}} = 0.3$ Myr. The jet is light with a density contrast $\eta = 0.01$, which has been previously adopted in many jet simulations. Due to an additional CR component, the jet is over-pressured by a factor of ~ 10 with regard to the ambient hot gas at the jet base $z = z_{\text{jet}}$. Energetically the kinetic power in the jet dominates over the CR power by a factor of ~ 5 (see Table 2). The simulation is started at $t = 0$, and stopped at the current age of the *Fermi* bubbles $t = t_{\text{Fermi}} = 2.06$ Myr. The small value of $t_{\text{jet}}/t_{\text{Fermi}} \sim 0.15$ implies that all the CRs within the bubbles at the current time have nearly the same age, consistent with the *Fermi* observation that the gamma-ray spectral index is quite uniform across the whole *Fermi* bubbles (Su et al. 2010).

Figure 2 shows central slices of CR energy density (top panels) and thermal electron number density (bottom panels) in logarithmic scale at $t = 1$ Myr (left panels), and $t = t_{\text{Fermi}} = 2.06$ Myr (right panels). As clearly seen, the jet produces a rapidly expanding CR bubble, which roughly matches the current north *Fermi* bubble (dotted circle) at $t = 2.06$ Myr. The CR transport is dominated by advection due to the high velocity of thermal gas in the jet. The CR diffusivity in this run is low $\kappa = 3 \times 10^{27} \text{ cm}^2 \text{ s}^{-1}$, having a very small effect, which can also be seen by the sharp edge of the resulting CR bubble (see Section 3.2). The sharp edge is also an important feature of the observed *Fermi* bubbles. The lateral expansion of the bubble is mainly due to its high internal pressure (contributed by both CRs and shocked thermal gas) within the bubble and the rapidly decreasing ambient gas pressure with the galactocentric distance. The resulting CR bubble is much narrower if the initial jet has a smaller internal pressure. Due to the expansion, the gas density in the bubble is significantly lower than the ambient gas density, as clearly seen in the bottom panels of Figure 2. This explains why *ROSAT* X-ray observations show a ‘cavity’ of X-rays toward the center of

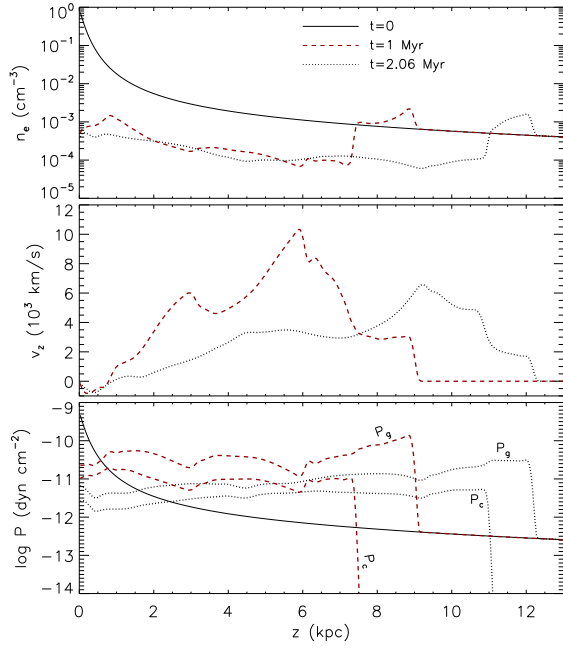


FIG. 3.— Variations of electron number density (top), the z -component gas velocity (middle), and pressures (bottom) along the jet axis for run A1 at $t = 1$ Myr (dashed) and $t = 2.06$ Myr (dotted). The initial gas density and pressure profiles along the z -axis at $t = 0$ are plotted as solid lines in the top and bottom panels, respectively.

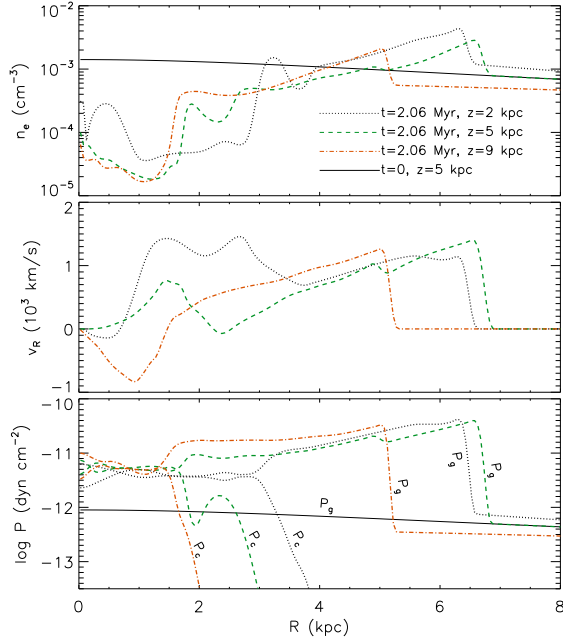


FIG. 4.— Variations of electron number density (top), the R -component gas velocity (middle), and pressures (bottom) along the R -direction (perpendicular to the jet axis) for run A1 at $t = 2.06$ Myr at $z = 2$ (dotted), 5 (dashed), and 9 kpc (dot-dashed). The initial gas density and pressure profiles along the R -direction at $z = 5$ kpc are plotted as solid lines in the top and bottom panels, respectively.

the *Fermi* bubbles (similar to X-ray cavities often found in galaxy clusters).

The bottom panels of Figure 2 show a strong shock produced by the jet activity. The shock propagates into the hot Galactic halo, and at $t = t_{\text{Fermi}}$ (i.e., the time when

the bubbles are currently being observed), has a speed of ~ 2000 km/s (mach number $M \sim 9$) at the north-most shock front. The propagating shock can also be seen in Figure 3, which shows variations of thermal electron number density, the z -component of the gas velocity v_z , and pressures along the jet axis at $t = 1$ Myr and $t = 2.06$ Myr. In directions perpendicular to the jet axis, the shock has a slightly smaller speed, reaching $R \sim 6$ kpc at $t = t_{\text{Fermi}}$, as seen in Figure 2. Combining with the shock propagating toward the south direction, the *Fermi* bubble event produced a dumbbell-shaped shock front. The shocked gas near the shock front has higher densities ($n_e \sim 1 - 4 \times 10^{-3} \text{ cm}^{-3}$) and temperatures ($T \sim 3 - 7$ keV), potentially explaining the dumbbell-shaped X-ray shell features detected by the *ROSAT* X-ray telescope (Sofue 2000; Bland-Hawthorn & Cohen 2003). The *ROSAT* X-ray shell feature is most prominent in the northeastern direction (the North Polar Spur; see Fig. 1 in Sofue 2000), and its outer edge shown as the dashed line in Figure 2 is roughly spatially coincident with the shock front in the same direction. At $t = t_{\text{Fermi}}$, the shock front in the East direction has a speed of ~ 1800 km/s. At a distance of $R_{\odot}/\cos(35^\circ) \approx 10.4$ kpc, the shock front (i.e., the outer edge of the X-ray feature) requires about 27 yrs to move an arcsecond, the approximate resolution of the *Chandra* X-ray Telescope. Our jet model can not reproduce the bi-conical structure in the *ROSAT* 1.5 keV map as shown in Figure 5(d) of Bland-Hawthorn & Cohen (2003), which is located within the *Fermi* bubbles and may be produced by a more recent nuclear event.

The strong shock ($M \sim 8 - 9$) shown in Figures 2, 3 and 4 indicates that the *Fermi* bubbles are expanding explosively, only slightly decelerated by the small inertial resistance of the surrounding halo gas. The average total pressure inside our computed *Fermi* bubbles is about 50 - 100 times larger than that in the un-shocked ambient halo gas. This is very different compared to radio bubbles and X-ray cavities in galaxy clusters, where usually weak shocks with Mach number $M \sim 1 - 2$ are induced. Furthermore, buoyancy which is widely recognized to play a key role in the evolution of X-ray cavities in many galaxy clusters, is much less important in the evolution of our simulated *Fermi* bubbles, where the momentum and energy injected by the jets play the dominant role.

The internal structure of the CR bubble can be seen in Figure 4, which shows variations of electron number density, the R -component gas velocity v_R , and pressures along the R -direction (perpendicular to the jet axis) at $t = 2.06$ Myr at three different heights: $z = 2$ (dotted), 5 (dashed), and 9 kpc (dot-dashed). The bubble corresponds to regions with high CR pressure, and is surrounded by the outward-propagating shock represented by large jumps in n_e , v_R and P_g , which show the structure of the shock visible in Figure 2. The bubble has low gas densities $n_e \sim 1 - 8 \times 10^{-5} \text{ cm}^{-3}$, and is separated from the surrounding shocked gas through a contact discontinuity across which the total pressure is continuous. Within the bubble, the CR pressure in run A1 is typically $\sim 3 - 6 \times 10^{-12} \text{ dyn cm}^{-2}$, which is comparable to the gas pressure, and slightly larger than the magnetic pressure of the $5 - 10 \mu\text{G}$ fields considered by Su et al. (2010) to explain the “WMAP haze” observed at the base of the *Fermi* bubbles as synchrotron emission. This supports

our neglect of the magnetic field in the bubble dynamics, which will likely not significantly change our results. However, as discussed in the last paragraph of Section 3.3, the CR pressure in our simulated bubbles depends on a model parameter – the initial CR pressure at the jet base, and does not represent the real CR pressure in the *Fermi* bubbles, which may be constrained by microwave and gamma ray emissions from the bubbles (see Sec. 3.5).

In run A1, the jet is energetically dominated by the kinetic energy, with the kinetic power $P_{\text{ke}} \sim 7.09 \times 10^{43}$ erg s⁻¹ and the CR power $P_{\text{cr}} \sim 1.43 \times 10^{43}$ erg s⁻¹. The total jet power is $P_{\text{jet}} \sim 8.6 \times 10^{43}$ erg s⁻¹. The jet is assumed to be produced by Sgr A*, the supermassive black hole located at the GC. Taking a standard accretion efficiency of 10%, the black hole accretion rate can be determined $\dot{M}_{\text{BH}} = 2P_{\text{jet}}/(0.1c^2) = 0.03 M_{\odot}/\text{yr}$ (note that the black hole ejects two opposing jets). During this AGN event ($0 \leq t \leq t_{\text{jet}} = 0.3$ Myr), the black hole accreted a total of $\Delta M_{\text{BH}} \sim 9000 M_{\odot}$ gas, and ejected in the jets a total of $M_{\text{jet}} \sim 1.5 \times 10^5 M_{\odot}$ gas, which is estimated at $|z| = 0.5$ kpc and thus includes the potential gas entrained by the jets at $|z| < 0.5$ kpc (see Table 2). Assuming that Sgr A* has a mass of $M_{\text{BH}} \sim 4 \times 10^6 M_{\odot}$ (Ghez et al. 2008), the Eddington luminosity is $L_{\text{Edd}} \sim 5.5 \times 10^{44}$ erg s⁻¹, and the Eddington ratio for the AGN activity is $\epsilon = 2P_{\text{jet}}/L_{\text{Edd}} \sim 0.31$. However, as we discuss in Section 3.3, the energetics of the *Fermi* bubble event scales with the uncertain density of the ambient halo gas, which confines the bubbles. For example, if the normalization of the halo gas is lower by a factor of 10, the energy and power of the associated AGN event are also smaller by the same factor 10.

While the overall energetics, size, shape and age of our A1 *Fermi* bubble shown in the right panels of Figure 2 are encouraging, this bubble is deficient in two important respects that can be expected from any calculation based on the standard hydrodynamic equations 1 - 4. First, the pagoda-shaped bubble boundaries visible in Figure 2 – formed by a series of Kelvin-Helmholtz vortices – disagrees significantly with the globally smooth, egg-shaped gamma-ray bubbles observed with the *Fermi* telescope (Su et al. 2010). Second, the quasi-uniform distribution of CR electrons, proportional to $e_c(R, z)$ plotted in Figure 2, is inconsistent with the rather uniform gamma-ray surface brightness observed by *Fermi* across the bubble surfaces. The gamma-ray surface brightness produced by IC upscattering of rather smoothly distributed ISRF photons is roughly proportional to the integral of e_c along the line of sight through the bubble. For spatially uniform e_c , the surface brightness is expected to decrease significantly from the bubble center toward the boundaries at constant z where the ISRF photon density is roughly constant or decreases slightly in the same direction. Since the ISRF photon density is expected to decrease in the z -direction (away from the Galactic center), $e_c(R, z)$ must also increase in this direction. Consequently, to produce a gamma-ray image with uniform surface brightness, it is necessary that $e_c(R, z)$ increase smoothly toward all bubble boundaries. As we discuss below, these two observational discrepancies suggest that additional physics plays a significant role during the jet evolution. In Paper II, we show that these discrepancies

can be corrected by including gas viscosity.

3.2. Suppression of CR Diffusion across the Bubble Surface

In our fiducial run A1, we choose a constant CR diffusion coefficient $\kappa = 3 \times 10^{27}$ cm² s⁻¹, which is much lower than typical estimates of diffusivity in our Galaxy $\kappa \sim (3-5) \times 10^{28}$ cm² s⁻¹. A low value for κ is specifically chosen to produce the CR bubble with sharp edge, which is one of the main features in the observed *Fermi* bubbles. When the diffusivity is not strongly suppressed, the edges of the resulting CR bubble are usually very broad, inconsistent with observations. To study the effect of CR diffusion on the bubble evolution, we perform three additional runs A-diff1, A-diff2, and A-diff3, which are all the same as run A1, but with different prescriptions for the CR diffusivity κ .

In run A-diff1 and A-diff2, the CR diffusion coefficient is chosen to be $\kappa = 3 \times 10^{28}$, and 3×10^{29} cm² s⁻¹, respectively. In these cases, diffusion helps transport CRs, and thus the age of the CR bubble, $t_{\text{Fermi}} = 1.94, 1.30$ Myr respectively, is shorter than that in run A1. The 2D distribution of CR energy density at $t = t_{\text{Fermi}}$ in these runs is shown in left panels of Figure 5. When compared with run A1 (right-top panel), CR diffusion in runs A-diff1 and A-diff2 transports CRs to much large distances in the R direction, which is also clearly seen in Figure 6, which shows variations of CR pressure P_c along the R -direction at $t = t_{\text{Fermi}}$ at $z = 2$ (bottom), and 9 kpc (top) in runs A1, A-diff1, A-diff2, and A-diff3.

An important feature of the CR bubble produced in runs A-diff1 and A-diff2 is that the bubble edge is not sharp, as clearly seen in Figures 5 and 6. This feature is clearly produced by CR diffusion, which transports CRs across the bubble surface, rendering the *gradual* outward decline in CR energy density at bubble edges. When the CR diffusion coefficient is significantly suppressed as in our fiducial run A1, the CR bubble is mainly expanded due to CR advection, and has sharp edges. Observations of *Fermi* bubbles show that the bubble edge is very sharp (Su et al. 2010), suggesting that the CR diffusion is significantly suppressed. However, the CR diffusion coefficient may depend on the structure of local magnetic fields and may vary with space and time. One interesting question to ask is whether the sharpness of bubble edges implies that the CR diffusion is suppressed everywhere in the bubble regions (e.g., as in run A1). It is possible that the CR diffusion inside the bubble is not suppressed, as it does not directly affect the bubble surface. The key to produce sharp bubble edges is the suppression of CR diffusion across the bubble surface, which directly affects the structure of bubble edges. Physically, due to the small gyro-radii of relativistic particles (around 10^{-9} kpc for a 10 GeV electron in a $4 \mu\text{G}$ field), CR diffusion may be anisotropic and CRs diffuse mainly along magnetic field lines with cross-field diffusion strongly suppressed. During the creation of the CR bubbles, ambient gas just external to the bubbles is strongly compressed, resulting in tangential magnetic field lines near the surface. This may explain why CR diffusion is suppressed across the bubble surface. It will be of great interest in the future to study this issue in detail using magnetohydrodynamic simulations with anisotropic CR diffusion.

Without explicitly introducing magnetic fields, here we

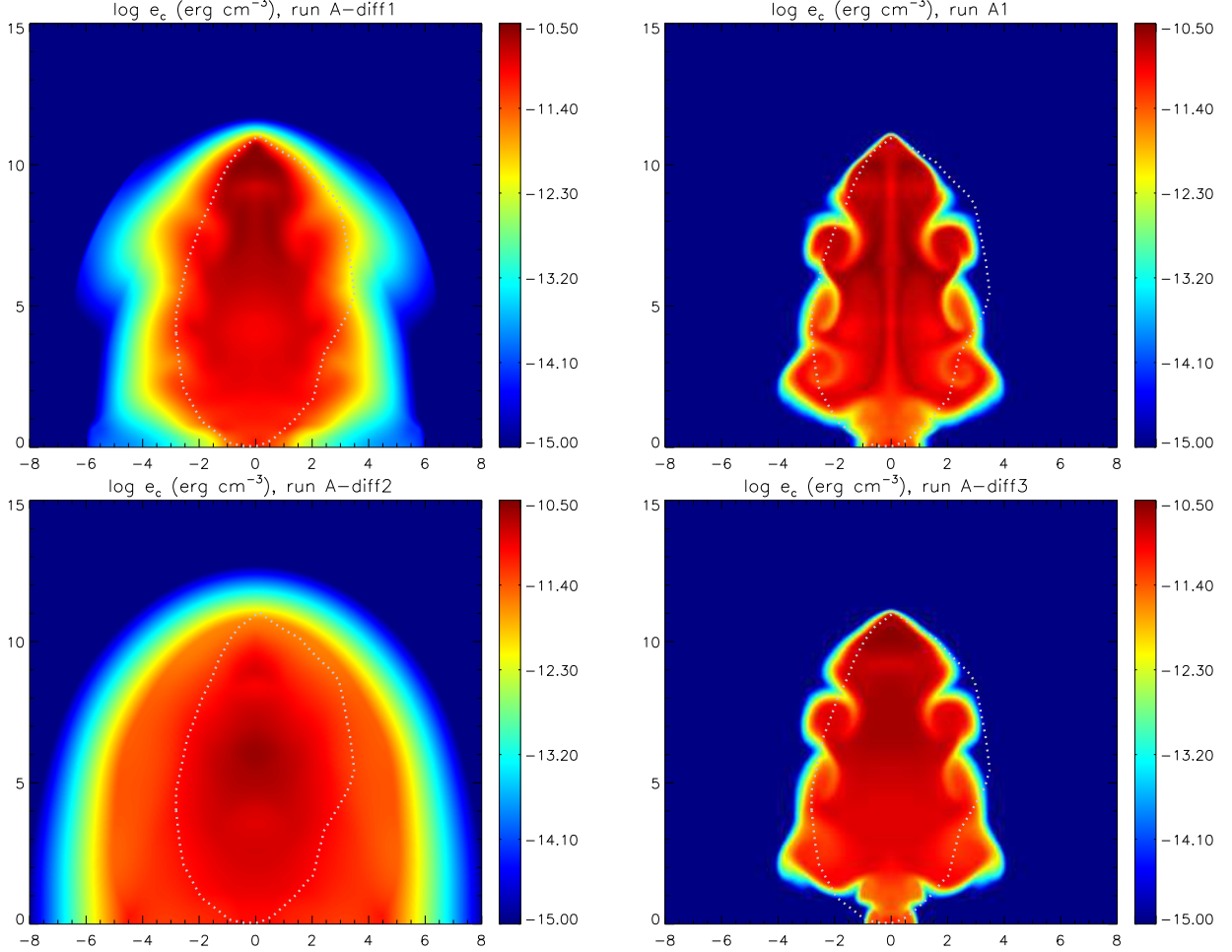


FIG. 5.— Central slices (16×15 kpc) of CR energy density in logarithmic scale in run A-diff1 (top-left), A1 (top-right), A-diff2 (bottom-left), and A-diff3 (bottom right) at $t = t_{\text{Fermi}}$ (details listed in Tables 1 and 2 for each run). Horizontal and vertical axes refer to R and z respectively, labeled in kpc. The dotted region in each panel encloses the observed north *Fermi* bubble. In runs A-diff1 and A-diff2, CR diffusion significantly affects the bubble evolution, rendering bubble edges that are less sharp than those observed. Variable CR diffusion in run A-diff3 leads to a smoother CR energy density distribution inside the bubble, while still suppressing CR diffusion across the bubble surface and retaining sharp bubble edges as in run A1.

want to do a preliminary study investigating how the CR bubble evolves if the CR diffusion is only suppressed across the bubble surface. To this end, we perform an additional run A-diff3, where the CR diffusion is normal ($\kappa \sim 10^{28} - 10^{29} \text{ cm}^2 \text{ s}^{-1}$) within the evolving CR bubble, but significantly suppressed exterior to the bubble surface. As shown in § 3.1, the CR bubble is separated from the surrounding thermal gas through a contact discontinuity, across which thermal gas density changes abruptly. Thus we assume that in run A-diff3, the CR diffusivity is related to thermal gas density through an ad-hoc equation:

$$\kappa = \begin{cases} 3 \times 10^{29} (n_{e0}/n_e) \text{ cm}^2 \text{ s}^{-1} & \text{when } n_e > n_{e0} \\ 3 \times 10^{29} \text{ cm}^2 \text{ s}^{-1} & \text{when } n_e \leq n_{e0}, \end{cases} \quad (13)$$

where $n_{e0} = 10^{-5} \text{ cm}^{-3}$. The parameters in equation 13 are chosen so that during the calculation of this run ($t \leq t_{\text{Fermi}}$), CR diffusion is always significantly suppressed outside the expanding bubble ($\kappa \lesssim 10^{28} \text{ cm}^2 \text{ s}^{-1}$), but not suppressed within it ($\kappa \sim 10^{28} - 10^{29} \text{ cm}^2 \text{ s}^{-1}$). The low CR diffusivity outside the bubble only suppresses CR diffusion across the bubble surface and does not directly affect regions much further away from

the bubble, since there are essentially no CRs there. At $t = t_{\text{Fermi}}$, the CR energy density distribution, shown in the bottom-right panel of Figure 5, is very similar to that in run A1 (top-right panel), and particularly, the edges of the CR bubble are also very sharp, indicating that the prescription for CR diffusivity shown in equation 13 indeed significantly suppresses CR diffusion across the bubble surface, and CR diffusion in the bubble interior is not required to be suppressed to produce the sharpness of the bubble edges. The bottom-right panel of Figure 5 also shows that the e_c distribution inside the bubble in run A-diff3 is much smoother than in run A1. CR diffusion inside the bubble removes local CR structures (e.g., regions with high or low CR energy densities as seen in the right-top panel of Fig. 5), which may otherwise have been seen in the *Fermi* observations of projected gamma-ray emission. The observed *Fermi* bubbles have approximately uniform surface brightness, which may imply that CR diffusion is not strongly suppressed inside the bubbles (i.e., only the CR diffusion across the bubble surface is strongly suppressed). Future data from even longer-duration *Fermi* observations are needed to study the possible internal structure of the *Fermi* bubbles.

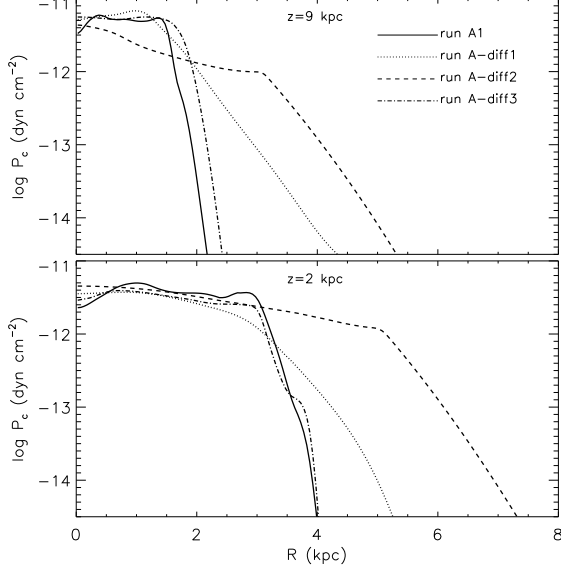


FIG. 6.— Variations of CR pressure P_c along the R -direction at $t = t_{\text{Fermi}}$ at $z = 2$ (bottom), and 9 kpc (top) in runs A1 (solid), A-diff1 (dotted), A-diff2 (dashed), and A-diff3 (dot-dashed). The edge of the CR bubble is not sharp in runs A-diff1 and A-diff2 because of CR diffusion across the bubble boundary.

3.3. A Parameter Study and Degeneracies

The jet simulation involves a large number of parameters, many of which are degenerate. It is thus impossible to uniquely determine all jet properties from the morphology of the observed *Fermi* bubbles. For example, a shorter jet duration t_{jet} results in a longer bubble age and a ‘fatter’ bubble, but this effect can be averted by a larger jet density n_{ej} , a higher jet velocity v_{jet} , or a smaller CR energy density e_{jcr} in the jet. Here we present results of a few additional (essentially degenerate) runs (A2, A3, and A4), all of which roughly produce the morphology of *Fermi* bubbles. The jet parameters and some results are summarized in Tables 1 and 2. Compared to run A1, the jet is more massive in run A2 ($\eta = 0.02$), faster in run A3 ($v_{\text{jet}} = 0.2c$), and narrower in run A4 ($R_{\text{jet}} = 0.2$ kpc). The age of *Fermi* bubbles in these runs is $t_{\text{Fermi}} = 1.74, 0.86, 2.34$ Myr respectively. The 2D distribution of CR energy density at $t = t_{\text{Fermi}}$ in these runs is shown in Figure 7, where the electron number density distribution in run A2 is also shown in the bottom-left panel. In run A2, the shock fits even better with the outer edge of the X-ray shell feature (dashed line) than in run A1, strengthening the point that the *ROSAT* X-ray features surrounding the *Fermi* bubbles are produced by shocked gas associated with the jet activity. These four runs are representative of successful jet models which roughly reproduce the overall size and shape of the *Fermi* bubbles, suggesting that the *Fermi* bubbles could be produced by a powerful AGN jet event which began about 1 - 3 Myr ago, and was active for a duration of $\sim 0.1 - 0.5$ Myr.

The evolution of AGN jets and the resulting CR bubbles also depend on the initial density of the confining halo gas. For a gaseous halo with fixed temperature, its initial hydrostatic density distribution can be scaled up or down by varying the central gas density n_{e0} . Equations 1 - 4 ensure that the evolution of the jet and resulting CR bubble is the same if the following three jet properties – density ρ_j , thermal energy density e_j and

CR energy density e_{jcr} are scaled by the same factor as n_{e0} . As an example, here we present the result of an additional run A5, where n_{e0} , ρ_j , e_j , and e_{jcr} are all scaled down by the same factor 100 with respect to run A1. The spatial distribution of CR energy density in this run at time $t = t_{\text{Fermi}}$ is shown in the top panel of Figure 8, confirming that the morphological evolution of the jet and bubble is the same as in run A1. It is important to note that the jet duration and the current age of the *Fermi* bubbles are not affected by the halo gas density, while the total jet energy and the CR energy density within the bubbles scale with it. Thus, due to our limited knowledge of the halo gas density, the energetics of the AGN event responsible for the *Fermi* bubbles – as well as the CR energy density and the gamma-ray emissivity – is not constrained very well by our model. Depending on the initial density distribution in the Galactic halo, the energetics of the *Fermi* bubble event may be $\sim 10^{55} - 10^{57}$ erg (Table 2).

In principle, accurate X-ray observations of the shell of shocked gas surrounding the *Fermi* bubbles can improve our estimate of the gas density distribution in the pre-bubble atmosphere and consequently the energetics of the dynamical event that created the bubbles. All-sky *ROSAT* X-ray observations at 0.75 and 1.5 keV were used by Sofue (2000) to identify dumbbell-shaped shells of soft X-ray emission having lobes about 10 kpc in diameter symmetric about the Galactic center and aligned approximately along the Galactic rotation axis. At the time Sofue (2000) interpreted this as emission from gas in the Galactic halo that was shocked by an explosion in the Galactic center with total energy $E_{\text{tot}} \sim 10^{56}$ erg that occurred about 1.5×10^7 yr ago. However the original atmosphere adopted by Sofue (2000) is considerably different (not in hydrostatic equilibrium) and about 18 times less dense than ours at $R = 0$, $z = 5$ kpc (Figure 1) near the bubble center. The corresponding single-bubble energy found by Sofue (2000), when scaled to our atmosphere, is $E_{\text{jet}} = 0.5E_{\text{tot}} \times 18 \approx 9 \times 10^{56}$ erg, which is consistent with our model A1 where $E_{\text{jet}} = 8 \times 10^{56}$ erg. Similar to the *Fermi* bubbles, the real energetics of the *ROSAT* X-ray shells is not well constrained due to the uncertain density of the original gas in the Galactic halo. However, if they were indeed produced by a jet event (e.g. the *Fermi* bubble event), their age may be much shorter than 15 Myrs as estimated in a starburst model by Sofue (2000).

The evolution of AGN jets and resulting bubbles depends on the total pressure in the initial jet, but it is insensitive to how the jet pressure is distributed between thermal and non-thermal components. Thus, another uncertainty in our dynamical model is the ratio of the CR to thermal pressure within the jet, which is directly related to an important problem – the particle content (thermal versus non-thermal) within the current *Fermi* bubbles. In run A1, the CR pressure dominates in the initial AGN jet (the ratio of CR to thermal pressure is 9.25), resulting in comparable CR and thermal pressures within the *Fermi* bubbles at the current time (see the bottom panel in Fig. 4). However, the CR-to-thermal pressure ratio in the bubbles depends on its initial value at the jet base, and is generally not 1 in our simulations. In an additional run A6, we follow the evolution of a jet

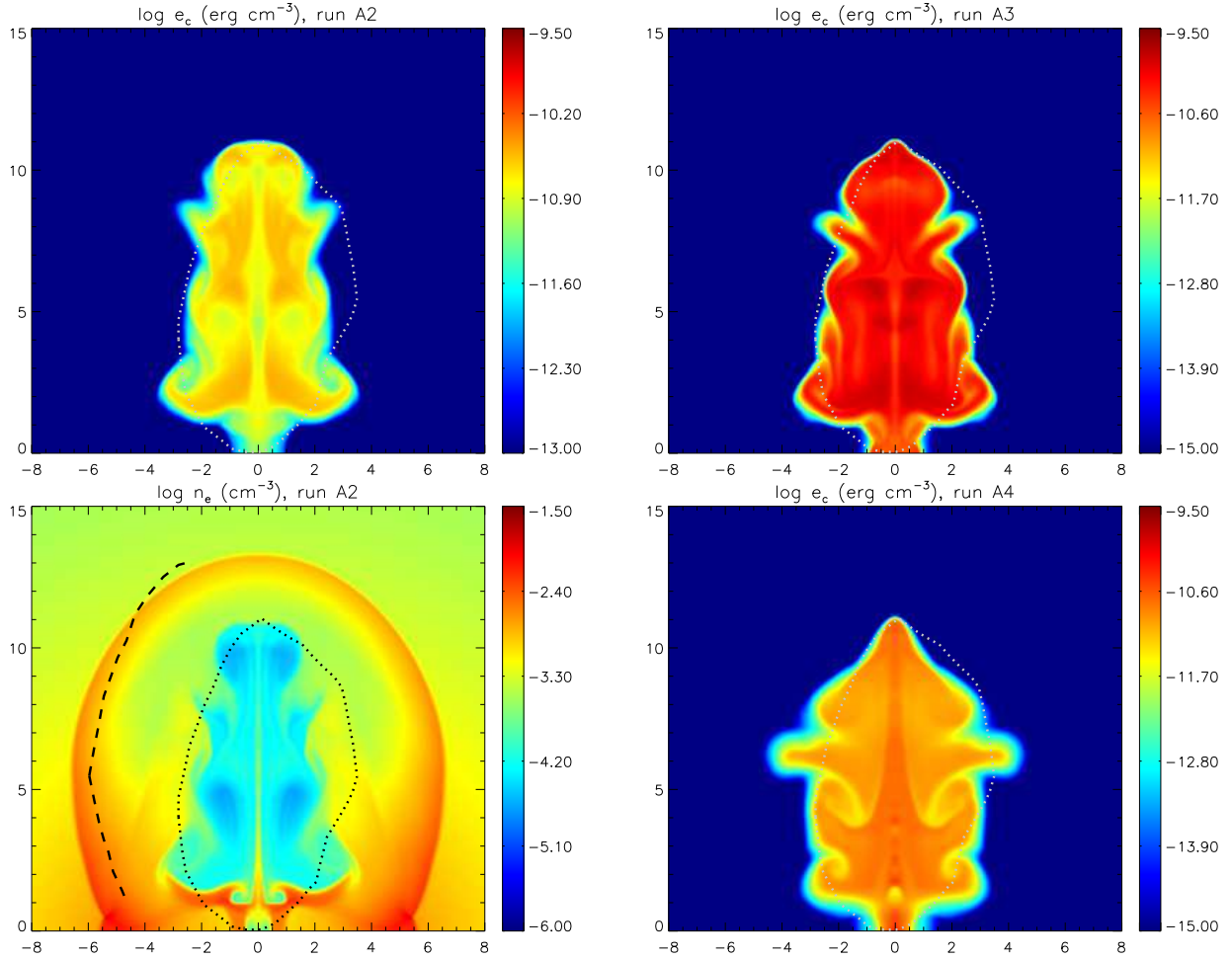


FIG. 7.— Central slices (16×15 kpc) of $\log(e_c)$ in run A2 (top-left), A3 (top-right), A4 (bottom-right), and $\log(n_e)$ in run A2 (bottom left) at $t = t_{\text{Fermi}}$ (details listed in Tables 1 and 2 for each run). Horizontal and vertical axes refer to R and z respectively, labeled in kpc. The dotted region in each panel encloses the observed north *Fermi* bubble. The dashed lines in the bottom-left panel trace the outer edge of the *ROSAT* X-ray emission feature surrounding the northern bubble. Run A1 and these additional runs have different jet parameters, but all produce CR bubbles approximately matching the observed *Fermi* bubbles.

dominated by thermal pressure (the initial ratio of CR to thermal pressure is ~ 0.1 ; the total jet pressure, jet density and other parameters are the same as run A1; see Table 1), finding that the morphological evolution of the resulting CR bubbles in this run is very similar to run A1, as clearly seen in the bottom panel of Figure 8. Due to much lower CR power in the initial jet, run A6 produces *Fermi* bubbles having proportionally lower CR pressure P_c (much lower than thermal pressure) and lower gamma ray surface brightness than our fiducial run A1. The CR pressure in our successful runs by no means represents the real CR pressure in the *Fermi* bubbles, which can be constrained by microwave and gamma ray emissions from the *Fermi* bubbles (see Sec. 3.5). However, our dynamical model is robust and the bubble evolution, which depends on the total jet pressure, is insensitive to the CR pressure. Analyses based on multi-wavelength (X-ray, gamma-ray, microwave, radio) observations of the *Fermi* bubbles and the surrounding gas, which is beyond the scope of this paper, should be used to constrain the density of halo gas and the particle content of the *Fermi* bubbles.

3.4. Constraints on the Jet Density

As discussed in the previous subsection, it is hard to accurately determine the jet properties, but it is possible to put some useful constraints, particularly on the jet density. When the jet is very light, e.g., $\eta = 0.0001$ as in run B1 (see Table 1 for other jet parameters), it quickly decelerates in the hot gas, and expands laterally in the R direction due to the high pressure within the bubble. The top panel of Figure 9 shows the CR energy density in logarithmic scale at $t = 3$ Myr. As clearly seen, the jet only reaches $z \sim 6$ kpc at this time, and the resulting CR bubble is quasi-spherical, unlike the observed *Fermi* bubbles elongated in the z direction. Very light jets tend to have strong backflows (i.e., with $v_z < 0$ inside the bubble at large R), which expand laterally, forming CR bubbles much ‘fatter’ than *Fermi* bubbles (see Guo & Mathews 2011). We have experimented with more runs with different jet densities, and find that the *Fermi* bubbles can be successfully reproduced only with jet densities $\eta \gtrsim 0.001$.

On the other hand, when the jet is very massive, e.g., $\eta = 0.5$ as in run B2 (see the bottom panel of Figure 9), it decelerates very slowly, producing very little backflow. In this case, most of the CRs are advected by the jet to the jet tip, not forming a ‘fat’, radially-elongated bubble as observed. We have run many simulations with high

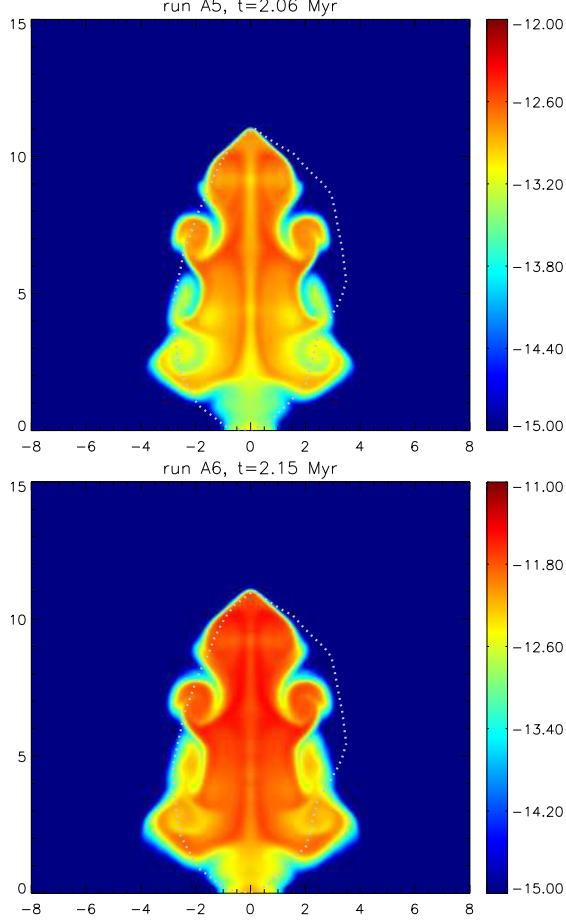


FIG. 8.— Central slices (16×15 kpc) of $\log(e_c)$ in run A5 (top) and A6 (bottom) at $t = t_{\text{Fermi}}$. Horizontal and vertical axes refer to R and z respectively, labeled in kpc. The dotted region in each panel encloses the observed north *Fermi* bubble. Run A5 shows that the required jet power and the CR energy density are proportionally smaller in a gaseous halo with lower densities compared to run A1, while run A6 shows that the morphological bubble evolution is quite insensitive to the relative contribution of CRs and thermal gas to the jet pressure when the total jet pressure and other model parameters are fixed.

jet densities, and found that the formed CR bubbles are usually much thinner than the observed *Fermi* bubbles. Acceptable runs typically have the jet density contrast $\eta \lesssim 0.1$.

AGN jets efficiently transport CRs from the GC to the Galactic halo. Additionally the jets can produce or re-accelerate CRs in the strong shock at the jet tip (hot spot) which we have not considered here. The morphology and evolution of the resulting CR bubble significantly depend on many jet properties, but the jet density contrast is particularly important. From the morphology of the *Fermi* bubbles, we can approximately constrain the jet density contrast: $0.001 \lesssim \eta \lesssim 0.1$, which corresponds to $6 \times 10^{-5} \text{ cm}^{-3} \lesssim n_{\text{ej}} \lesssim 6 \times 10^{-3} \text{ cm}^{-3}$ for our adopted model for the Galactic thermal atmosphere. The constraint on the jet density contrast η is quite robust, not depending on the value of $n_{\text{e}0}$, the density normalization of the ambient halo gas.

3.5. Success and Problems of Our Jet Model

The detection of the *Fermi* bubbles in the Galaxy is one of the biggest discoveries in astronomy in recent

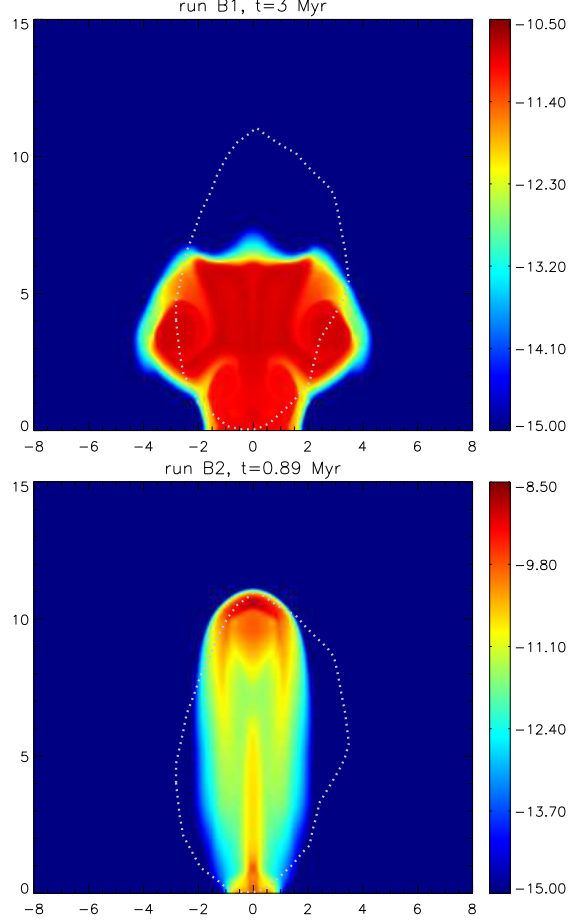


FIG. 9.— Central slices (16×15 kpc) of CR energy density in logarithmic scale in run B1 at $t = 3$ Myr (top) and B2 (bottom) at $t = t_{\text{Fermi}}$. Horizontal and vertical axes refer to R and z respectively, labeled in kpc. The dotted region in each panel encloses the observed north *Fermi* bubble. Very light jets in run B1 ($\eta = 0.0001$) decelerate rapidly in the halo gas, forming quasi-spherical CR bubbles unlike the radially elongated *Fermi* bubbles observed. On the other hand, the massive jets in run B2 ($\eta = 0.5$) transport most CRs just along the z axis, not forming the 'fat' bubbles observed.

years. The origin of the bubbles remains mysterious. Here we are proposing that the bubbles were produced by a recent powerful AGN jet event from the GC. We focus on the formation and dynamical evolution of the *Fermi* bubbles, leaving details of the multi-wavelength emission features to future work. In this subsection, we summarize the success and potential problems of our jet model in explaining the observed features of the *Fermi* bubbles.

Our model successfully explains a few key observational features of the *Fermi* bubbles. (1) The origin of CRs is naturally explained within a jet scenario. CRs can be accelerated to very high energies in AGN jets near supermassive black holes and/or in jet hotspots, as seen in numerous observations of extragalactic AGN jets. (2) Sub-relativistic jets naturally produce large CR bubbles within a few Myrs, a *short bubble age* inferred from the fact that the gamma-ray emission is likely dominated by the IC emission of CRes (Dobler et al. 2010 and Su et al. 2010). It is not trivial to transport or accelerate CRs in 10 kpc sized bubbles within such a short amount of time. (2) The opposing jet scenario naturally explains

the bilobular morphology of the bubbles, which are symmetric with respect to the GC. (3) We identified a few sets of jet parameters, with which the jets produce CR bubbles with morphologies similar to the observed bubbles (mainly the bubble elongation and ellipticity). (5) In our model, the jet duration is much shorter than the bubble age, implying that the CRs in the whole bubble have similar age at the current time. This explains the *Fermi* observation that the gamma ray spectral index is quite uniform across most regions of the two bubbles. (6) The jet event produces a strong shock, which heats and compresses the ambient gas in the Galactic halo, potentially explaining the *ROSAT* X-ray shell features surrounding the bubbles. (7) Sharp bubble edges indicate that the *Fermi* bubbles have been expanding mainly due to CR advection, while CR diffusion across bubble edges is strongly suppressed.

However, there are still some potential problems associated with our model, which need to be investigated in future studies. The main difference between the simulated CR bubble and the observed *Fermi* bubbles is that the former suffers from Kelvin-Helmholtz instabilities at its surface (as clearly seen in Figure 2), while the real *Fermi* bubbles have smooth edges. Line-of-sight projection tends to smooth the bubble edge when viewed in Galactic coordinates, but it is unable to completely remove surface irregularities created by these instabilities, as seen in Figure 10, which shows for run A1 the line-of-sight projection of CR energy density (a proxy for the gamma-ray surface brightness due to CR electrons) and ρ_{ec} (a proxy for the gamma-ray surface brightness originated from CR protons). This discrepancy suggests that there may be additional physics, which plays an important role in the bubble evolution, suppressing the development of these instabilities. Similar surface instabilities have received much attention in numerical studies of radio bubbles and X-ray cavities in galaxy clusters, where gas viscosity (Reynolds et al. 2005) and magnetic tension (Ruszkowski et al. 2007), have been invoked to successfully suppress these instabilities at the boundaries of buoyantly-rising bubbles. But it remains to be shown that the instabilities can also be suppressed during the creation of AGN bubbles. A preliminary study exploring the beneficial role of viscosity on the bubble evolution and morphology is presented in Paper II. Viscous suppression of instabilities in the *Fermi* bubbles may provide an unusual opportunity to study the interesting gas microphysics – viscosity – in hot plasma.

An interesting feature of the observed *Fermi* bubbles is the approximately uniform gamma-ray surface brightness, particularly at high latitudes ($|b| \gtrsim 30^\circ$). However, a nearly uniform CR distribution, as in our models computed here, produces a center-brightened (limb-darkened) surface brightness distribution in projection (see Figure 10), which is inconsistent with uniform gamma ray brightness observed in the *Fermi* bubbles. A flat surface brightness distribution implies that the CR density increases gradually toward bubble edges and with Galactic latitude from the bubble center. However, if CRs are too concentrated at the bubble surface, the gamma-ray surface brightness will be too strongly limb-brightened. Thus, the CR distribution may need some fine-tuning to get a roughly flat gamma-ray intensity. Although such an edge-favored CR distribution is not

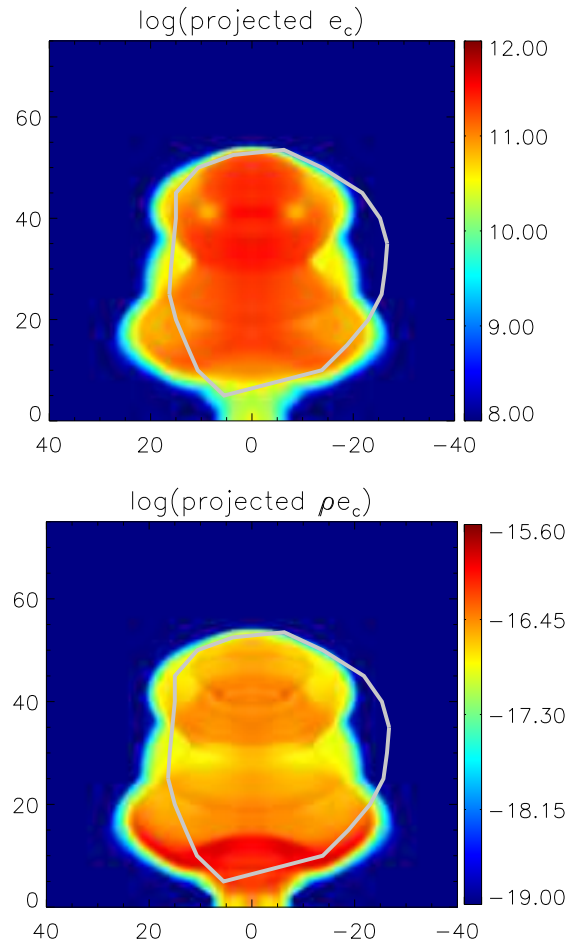


FIG. 10.— Line-of-sight projection of CR energy density (top; a proxy for the gamma-ray surface brightness due to CR electrons) and ρ_{ec} (bottom; a proxy for the gamma-ray surface brightness originated from CR protons) in logarithmic scale in run A1 at $t = 2.06$ Myr. Horizontal and vertical axes refer to Galactic longitude and latitude respectively, labeled in degrees. The solid circle represents the edge of the observed south *Fermi* bubble. Edge irregularities and edge darkening are clearly seen at high latitudes. At low latitudes ($|b| \lesssim 20^\circ - 30^\circ$), *Fermi* observations are significantly contaminated by emissions from the Galactic disk and bulge. The spatial variations of CR spectra and ISRF may affect the gamma-ray map, which is not considered here.

reproduced in our current jet simulations, this discrepancy does not invalidate the jet scenario for the *Fermi* bubbles. Instead, it may require a new physical mechanism that operates additionally in the standard AGN jet model. In Paper II, we argue that hot gas viscosity may provide the additional physics to suppress surface irregularities and to produce an edge-favored CR distribution, resulting in a more uniform gamma ray surface brightness distribution. Other physical mechanisms (e.g., stochastic re-acceleration of CR electrons preferentially near bubble edges as suggested by Mertsch & Sarkar 2011) may also contribute to surface brightness uniformity.

In this paper, we choose a very simple model for the ambient gas distribution – a hot volume-filling isothermal gas in hydrostatic equilibrium. In reality, the gas distribution in the Galaxy may be much more complex. Gas motions (e.g. winds) may be present, producing non-axisymmetric features in the bubble morphology. At low latitude, the hot, warm and cold gas within and near the Galactic bulge may significantly affect the jet evolution

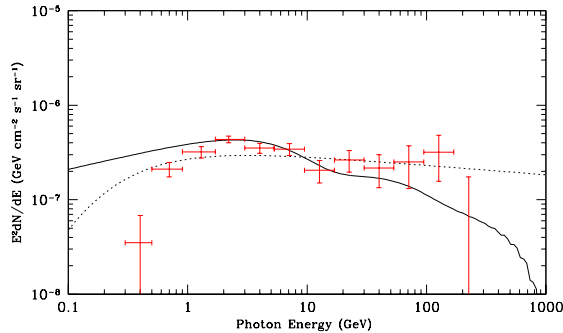


FIG. 11.— Gamma-ray spectrum from a CR electron population (IC scattering; solid line) and a CR proton population (pion decay; dashed line). The CRe spectrum is taken to be a power law in energy: $dN/dE \propto E^{-2.4}$ with $0.1 \leq E \leq 1000$ GeV. The CR proton spectrum is assumed to be a power-law in momentum: $dN/dp \propto p^{-2.1}$ with $0.1 \leq p/m_{\text{pc}} \leq 1000$. Crosses represent the observed average gamma ray flux from the *Fermi* bubbles (Su et al. 2010).

and the bubble shape there. Some of our current simulations produce a ‘stem’ feature at low latitude (see Fig. 2), which can not be accurately studied without modeling the multi-phase gas there. Due to strong gamma-ray contaminations from the Galactic disk and bulge at low latitude, further studies are required to investigate if the stem is indeed present or not in the observed *Fermi* bubbles.

With hydrodynamic simulations, we focus on the evolution and morphology of the *Fermi* bubbles in this paper. Our simulations also investigate the transport of CRs (advection and diffusion) by following the evolution of the CR energy density e_c , which may be contributed by CR electrons and/or protons with arbitrary spectra. The real CR content and spectrum in the *Fermi* bubbles may be constrained by the observed gamma ray spectrum, which is being actively studied and debated in the literature (e.g. Su et al. 2010; Crocker & Aharonian 2011). Here we present simple emission calculations in two extreme cases, assuming that the gamma ray flux is emitted entirely by CR electrons and protons respectively. In the leptonic scenario, we follow Su et al. (2010), adopting a power-law electron spectrum $dN/dE \propto E^{-2.4}$ with $0.1 \leq E \leq 1000$ GeV. We choose the normalization of the electron spectrum so that the calculated gamma ray spectrum, which is shown as the solid line in Figure 11, is roughly consistent with the observed gamma ray luminosity. Here we used the Klein-Nishina IC cross section (Blumenthal & Gould 1970) and an approximate line-of-sight integration length of 4 kpc across the bubbles. The ISRF model is taken from the latest version (version 54.1.984) of GALPROP (evaluated at the bubble center $R = 0$, $|z| = 5$ kpc). We also calculated synchrotron emission from CR electrons in this model and found that, when the magnetic field strength in the bubbles is chosen to be $8 \mu\text{G}$, the synchrotron flux at 23 GHz is around 1.1 kJy/sr , consistent with the detected WMAP flux at around $b \sim -20^\circ - -30^\circ$. It remains unclear why the microwave flux from the south bubble drops significantly at $b \lesssim -35^\circ$ (see Dobler 2012).

Combining with our simulations, emission calculations may provide new insights on the *Fermi* bubbles. To this end, we calculated the CR pressure contributed by electrons between 0.1 and 1000 GeV in the above leptonic

model and found that it is around $P_e = 2.0 \times 10^{-15} \text{ dyn cm}^{-2}$, which is about four orders of magnitude below the total pressure ($\sim 10^{-11} \text{ dyn cm}^{-2}$) inside the simulated *Fermi* bubbles in run A1 (see Figs 3 and 4). This result is quite robust with respect to the power index of the electron spectrum, suggesting that the pressure within the *Fermi* bubbles is not dominated by CR electrons in the leptonic scenario. The dominant bubble pressure may instead come from thermal gas (e.g. in run A6), CR protons, or magnetic fields.

In the hadronic scenario, the gamma ray emission of the *Fermi* bubbles is dominated by the decay of neutral pions produced from hadronic collisions of CR protons with thermal nuclei (Crocker & Aharonian 2011). We assume that CR protons have a power-law distribution in momentum: $dN/dp \propto p^{-2.1}$ with $0.1 \leq p/m_{\text{pc}} \leq 1000$. We use an analytic formula in Enflin et al. (2007, eq. 62) to approximate gamma-ray emissivity from pion-decay and adopt thermal electron density in the *Fermi* bubbles to be 10^{-4} cm^{-3} (as in run A1; Figs 3 and 4), which was used to derive the target nucleon density. The resulting gamma-ray flux is shown in Figure 11 (dotted line) and the CR proton pressure in this model is $P_p = 5.1 \times 10^{-11} \text{ dyn cm}^{-2}$, slightly larger than the total pressure ($\sim 10^{-11} \text{ dyn cm}^{-2}$) inside the simulated *Fermi* bubbles in run A1. This does not rule out the hadronic scenario, since (1) the required CR proton pressure drops if the thermal gas density in the bubbles is higher and (2) the total bubble pressure in our dynamical simulations increases if the initial ambient gas pressure is larger. However, our simple calculations suggest that the required CR proton pressure in the hadronic scenario may dominate the total pressure in the bubbles, and is much larger than the CR electron pressure in the leptonic scenario.

4. SUMMARY AND IMPLICATION

The detection of *Fermi* bubbles in the Galaxy is one of the most important and striking findings during the first two years’ observations of the *Fermi Gamma-ray Space Telescope*. The bubbles are symmetric about the GC, with one above and the other below the Galactic plane. The surface brightness in γ -ray emission from the bubbles is quite uniform with sharp edges at the bubble boundaries. These observed properties make it very difficult to explain the bubbles in many of the standard ways, for example by supernova shocks in the Galactic plane or by dark matter annihilations.

The unique location, morphology, and sharp gamma-ray edges of the bubbles suggest that they were probably created by an episode of energy injection in the GC. Gamma rays from the bubbles can be produced by CR electrons and/or protons. Motivated by numerous double radio sources and X-ray cavities observed in other galaxies, we investigate in this paper if AGN jets from the GC can create the *Fermi* bubbles with the observed morphology, size and appropriate age. In our model, a pair of bipolar jets were released from the GC along the rotation axis of the Galaxy. We model the jet evolution using a series of 2D axisymmetric hydrodynamical simulations, following the evolution of CRs and their dynamical interactions with thermal gas (see Section 2.2). CR advection is modeled self-consistently and CR diffusion is also considered.

We show that the observed *Fermi* bubbles could be reproduced by a recent AGN jet event about 1 - 3 Myr ago, which was active for a duration of $\sim 0.1 - 0.5$ Myr. The total jet energy released during the AGN event may be $\sim 10^{55} - 10^{57}$ erg, depending on the initial density distribution of the hot halo gas which confines the bubbles. Containing both thermal gas and CRs, the two-fluid jet quickly advects CRs to high latitude. The jet is energetically dominated by the kinetic energy, and over-pressured with either CR or thermal pressure which induces lateral expansion, creating a fat CR bubble as observed. In our fiducial run A1, the two opposing jets have a total power of $2P_{\text{jet}} \sim 1.7 \times 10^{44}$ erg s $^{-1}$, corresponding to an accretion rate of $\dot{M}_{\text{BH}} \sim 0.03 M_{\odot}/\text{yr}$ for the central black hole and an Eddington ratio of $\epsilon \sim 0.31$. The jet activity also induces a strong dumbbell-shaped shock (currently Mach number $M \sim 8 - 9$), which heats and compresses the ambient gas in the Galactic halo, qualitatively similar to the dumbbell-shaped X-ray shell features observed by the *ROSAT* X-ray telescope.

The two observed *Fermi* bubbles are roughly located and elongated along the rotation axis of the Galaxy. In the jet scenario, this morphology requires that the two opposing jets that produced the *Fermi* bubbles were ejected nearly along the Galactic rotation axis, as assumed in our simulations. This jet direction may be possible if the gas accreted by Sgr A* had angular momentum in this direction or Sgr A* had a relatively strong spin along this direction before the accretion. It is unclear if this special orientation observed in the *Fermi* bubbles is a coincidence or a general feature of CR bubbles in disk galaxies (see Baum et al. 1993 for the same preferential orientation detected in radio bubbles in Seyfert galaxies).

Because of the degeneracy of successful bubble models with different jet parameters, it is difficult or impossible to determine unique jet parameters directly from the bubble location and morphology. However, we can put some useful constraints on them, particularly on the jet density contrast relative to the ambient hot gas at the jet base. Very low density, ultra-light jets decelerate quickly and usually form quasi-spherical bubbles unlike the observed *Fermi* bubbles which are radially elongated. In contrast, heavy, massive jets decelerate very slowly, advecting most CRs to the tip of the jet with too little lateral expansion. Successful jets are moderately light, having typical density contrasts $0.001 \lesssim \eta \lesssim 0.1$ (i.e., $6 \times 10^{-5} \text{ cm}^{-3} \lesssim n_{\text{ej}} \lesssim 6 \times 10^{-3} \text{ cm}^{-3}$ for our adopted model for the Galactic thermal atmosphere).

We also show that to produce sharp edges of the bubbles, CR diffusion across the bubble surface must be suppressed significantly below the CR diffusion rate observed in the solar vicinity. CR advection is responsible for the spatial expansion of the *Fermi* bubbles, which compresses thermal gas near the bubble surface, aligning the local magnetic fields to be tangential to the bubble boundary. CR diffusion is probably anisotropic, with cross-field diffusion strongly suppressed. However, it is likely that CR diffusion deeper inside the bubbles is not suppressed and it tends to remove small CR structures, resulting in a smoother CR distribution and γ -ray emission within the bubbles as suggested by *Fermi* observations.

The total pressure inside the *Fermi* Bubbles must not be less than the pressure of CRs required to produce the gamma ray emission observed. If the gamma-ray emission from the bubbles is mainly due to CR electrons, the required CR electron pressure to produce the observed gamma-ray flux is negligible compared to the total bubble pressure, which may instead be dominated by other components, e.g., thermal gas, CR protons, or magnetic fields. On the other hand, if the gamma-ray emission is mainly due to CR protons, the required CR proton pressure is much higher, probably dominating the total bubble pressure.

The *Fermi* bubbles provide plausible evidence for a recent powerful AGN jet activity in the Milky Way. Extragalactic jets have been detected in many distant galaxies, such as the famous jet in M87 (Junor et al. 1999; Kovalev et al. 2007). Numerous bipolar radio bubbles and X-ray cavities have also been observed, clearly associated with the central stellar bulges of massive galaxies. These non-thermal regions are almost certainly produced by AGN jets, which are often not detectable because of the short time when they are active (McNamara & Nulsen 2007). Multi-wavelength studies show that AGN jet activity deposits large amounts of mechanical and CR energy into the host environments, significantly affecting the evolution of gas and host galaxies. But in our Galaxy there has been little evidence for a currently-active AGN jet. It would be very unusual if Sgr A* has always been quiescent in the past, as during its growth, a large amount of energy ($\sim 0.1 M_{\text{BH}} c^2 \sim 10^{60}$ erg) may have been released. The detection of *Fermi* bubbles as the remnant of a recent powerful AGN jet event is thus of dramatic astronomical importance, suggesting that AGN jet activity may also happen regularly in our Galaxy.

Furthermore, AGN activity from the GC may contribute significantly to, or dominate, the CR population in the Galactic halo. Suppose for example that new pairs of *Fermi* bubbles with total CR energy 2.7×10^{56} ergs (twice that of the single bubble in run A1) are produced every 30 Myr (AGN duty cycle $\sim 1\%$). This would supply CR energy to the Galactic halo at a rate 2.86×10^{41} ergs s $^{-1}$. By comparison, if one supernova of energy 10^{51} ergs occurs in the Galaxy every 50 years and 10% of that energy is converted to CRs, the total CR power generated, 0.6×10^{41} ergs s $^{-1}$, is considerably less than the estimated rate from AGN activity. Nevertheless, CRs from previous generations of *Fermi* bubbles may not contribute significantly to the locally observed CR energy density – this would require that CRs return to the solar vicinity by relatively slow diffusion in the halo before buoyancy and kinetic energy of the moving bubbles carry them entirely out of the Galactic halo.

Do similar *Fermi* bubbles exist in other galaxies? Due to the limited sensitivity and resolution of gamma-ray observations, the *Fermi* telescope can not easily detect extragalactic *Fermi* bubbles similar to those in the Milky Way. However synchrotron emission of many bubbles has been detected and spatially resolved in radio observations. AGN jets have been observed in many spiral Seyfert galaxies where extended kpc-scale radio structures (KSRs) are common (Gallimore et al. 2006). In a sample of 12 Seyfert KSRs, Baum et al. (1993) found

that the extended radio emission tends to align with the projected minor axis of the host galaxy, similar to the orientation of the *Fermi* bubbles with respect to the Galactic disk (see Elmouttie et al. 1998 and Kharb et al. 2006 for two well-studied examples). It remains to be determined if the *Fermi* bubbles and extragalactic KSRs are indeed similar astrophysical phenomena.

Finally, as in Sections 3.1 and 3.5, we draw attention to two shortcomings of our CR+hydrodynamic computations of the *Fermi* bubble evolution: surface irregularities and non-uniform gamma ray limb darkening. Irregularities in the bubble boundaries are induced by instabilities in the differentially shearing flow between vertically downflowing gas in the bubbles and the (assumed) initially stationary gas in the Galactic halo. In addition, the rather uniform distribution of cosmic ray energy density

inside our computed bubbles would produce IC gamma ray intensities that decrease toward the bubble boundaries, assuming that the ISRF photons (which are up-scattered) are smoothly distributed. These inadequacies may suggest that a new physical mechanism in addition to the basic jet hydrodynamics, such as shear viscosity discussed in the companion paper – Paper II, plays a role during the evolution of the *Fermi* bubbles

FG thanks Fabrizio Brighenti, Gregory Dobler, Matthew McQuinn, S. Peng Oh and Aristotle Socrates for helpful discussions. We thank the anonymous referee for an insightful report. Studies of AGN feedback and the *Fermi* bubbles at UC Santa Cruz are supported by NSF and NASA grants for which we are very grateful.

REFERENCES

- Baum, S. A., O’Dea, C. P., Dallacassa, D., de Bruyn, A. G., & Pedlar, A. 1993, *ApJ*, 419, 553
- Blandford, R. D., & Rees, M. J. 1974, *MNRAS*, 169, 395
- Bland-Hawthorn, J., & Cohen, M. 2003, *ApJ*, 582, 246
- Blumenthal, G. R., & Gould, R. J. 1970, *Reviews of Modern Physics*, 42, 237
- Breitschwerdt, D., McKenzie, J. F., & Voelk, H. J. 1991, *A&A*, 245, 79
- Crocker, R. M., & Aharonian, F. 2011, *Physical Review Letters*, 106, 101102
- Dobler, G. 2012, *ApJ*, 750, 17
- Dobler, G., & Finkbeiner, D. P. 2008, *ApJ*, 680, 1222
- Dobler, G., Finkbeiner, D. P., Cholis, I., Slatyer, T., & Weiner, N. 2010, *ApJ*, 717, 825
- Elmouttie, M., Haynes, R. F., Jones, K. L., Sadler, E. M., & Ehle, M. 1998, *MNRAS*, 297, 1202
- Enßlin, T. A., Pfrommer, C., Springel, V., & Jubelgas, M. 2007, *A&A*, 473, 41
- Finkbeiner, D. P. 2004, *ApJ*, 614, 186
- Gallimore, J. F., Axon, D. J., O’Dea, C. P., Baum, S. A., & Pedlar, A. 2006, *AJ*, 132, 546
- Ghez, A. M., et al. 2008, *ApJ*, 689, 1044
- Guo, F., & Mathews, W. G. 2010a, *ApJ*, 712, 1311
- . 2010b, *ApJ*, 717, 937
- . 2011, *ApJ*, 728, 121
- Guo, F., Mathews, W. G., Dobler, G., & Oh, S. P. 2012, *ApJ* in press (arXiv: 1110.0834)
- Guo, F., & Oh, S. P. 2008, *MNRAS*, 384, 251
- Helmi, A., & White, S. D. M. 2001, *MNRAS*, 323, 529
- Junor, W., Biretta, J. A., & Livio, M. 1999, *Nature*, 401, 891
- Kharb, P., O’Dea, C. P., Baum, S. A., Colbert, E. J. M., & Xu, C. 2006, *ApJ*, 652, 177
- Kovalev, Y. Y., Lister, M. L., Homan, D. C., & Kellermann, K. I. 2007, *ApJ*, 668, L27
- Kulsrud, R. M. 2005, *Plasma physics for astrophysics* (Princeton University Press, Princeton, NJ)
- Laing, R. A., Canvin, J. R., Bridle, A. H., & Hardcastle, M. J. 2006, *MNRAS*, 372, 510
- Longair, M. S., Ryle, M., & Scheuer, P. A. G. 1973, *MNRAS*, 164, 243
- Martin, C. L. 2005, *ApJ*, 621, 227
- Mathews, W. G. 2009, *ApJ*, 695, L49
- Mathews, W. G., & Brighenti, F. 2008a, *ApJ*, 676, 880
- . 2008b, *ApJ*, 685, 128
- Mathews, W. G., & Guo, F. 2010, *ApJ*, 725, 1440
- McNamara, B. R., & Nulsen, P. E. J. 2007, *ARA&A*, 45, 117
- Mertsch, P., & Sarkar, S. 2011, *ArXiv e-prints*
- Reynolds, C. S., McKernan, B., Fabian, A. C., Stone, J. M., & Vernaleo, J. C. 2005, *MNRAS*, 357, 242
- Rupke, D. S. N., & Veilleux, S. 2011, *ApJ*, 729, L27+
- Ruszkowski, M., Enßlin, T. A., Brügggen, M., Heinz, S., & Pfrommer, C. 2007, *MNRAS*, 378, 662
- Scheuer, P. A. G. 1974, *MNRAS*, 166, 513
- Skilling, J. 1971, *ApJ*, 170, 265
- Sofue, Y., 2000, *ApJ*, 540, 224
- Stone, J. M., & Norman, M. L. 1992, *ApJS*, 80, 753
- Strickland, D. K., & Heckman, T. M. 2009, *ApJ*, 697, 2030
- Strong, A. W., & Moskalenko, I. V. 1998, *ApJ*, 509, 212
- Strong, A. W., Moskalenko, I. V., & Ptuskin, V. S. 2007, *Annual Review of Nuclear and Particle Science*, 57, 285
- Su, M., Slatyer, T. R., & Finkbeiner, D. P. 2010, *ApJ*, 724, 1044
- Wolfire, M. G., McKee, C. F., Hollenbach, D., & Tielens, A. G. G. M. 1995, *ApJ*, 453, 673
- Yao, Y., & Wang, Q. D. 2005, *ApJ*, 624, 751